

ARGONNE NATIONAL LABORATORY
9700 South Cass Avenue
Argonne, Illinois 60439

ANL/APS/TB-48

LCLS Prototype Undulator Report

Roger J. Dejus, Editor
Experimental Facilities Division
Advanced Photon Source

January 2004

work sponsored by
U.S. DEPARTMENT OF ENERGY
Office of Science

Table of Contents

1	INTRODUCTION	1
2	UNDULATOR REQUIREMENTS	1
2.1	LCLS Undulator Specifications	2
2.2	FEL Performance-Driven Tolerances	3
2.2.1	End-Phase Compensation	3
3	DESIGN AND ASSEMBLY	6
3.1	Introduction	6
3.2	Magnetic Design	7
3.3	Mechanical Design	8
3.3.1	Requirements	9
3.3.2	Mechanical Tolerances	9
3.3.3	Design Features	10
3.3.4	Choice of Housing Material	12
3.3.5	Base Plate (Six Piece)	13
3.3.6	Poles (with “Wings”)	14
3.3.7	Clamps	15
3.3.8	“Push-Pull” Screws and Incremental Shims for Gap Adjustment	16
3.3.9	Remotely Adjustable End-Gaps	16
3.3.10	Pole Side and Phase Shims	17
3.3.10.1	Bar Pole Side Shims (Trajectory Shims)	18
3.3.10.2	Phase Shims	20
3.3.10.3	Pole Side Shims (for Horizontal Magnetic Field)	20
3.3.11	Magnetic Shields	20
3.3.12	Cam Shaft Movers for Undulator Alignment	21
3.4	Assembly of Magnetic Structure	24
3.4.1	Sorting	24
3.4.1.1	Magnet Blocks	24
3.4.1.2	Poles	26
3.4.2	Assembly Process	28
3.4.3	Special Jig	28
4	TUNING AND MEASUREMENTS	29
4.1	Introduction	29
4.2	Magnetic Measurement Facility	29
4.2.1	Hall Probes	29
4.2.1.1	Temperature Dependence	29

4.2.1.2	Horizontal Magnetic Field Measurement.....	31
4.2.2	Measurement Accuracy.....	31
4.3	Measurements of the Assembled Prototype.....	32
4.3.1	Pole Gap.....	32
4.3.2	Trajectory and rms Phase Error.....	34
4.3.3	Temperature Dependence.....	36
4.3.4	Gap Dependence.....	37
4.3.5	Mechanical Stability.....	39
4.3.6	End-Phase Tuning.....	40
5	SUMMARY.....	44
5.1	Magnetic Design.....	44
5.2	Mechanical Design.....	44
5.3	Tuning and Measurements.....	45
5.4	Mechanical Modifications for the First Article.....	46
5.4.1	Revised Mechanical Tolerances.....	46
5.4.2	Aluminum Base Plate.....	46
5.4.3	End Phasing.....	46
5.4.4	Cam-Shaft Movers.....	47
5.4.5	New Support Pillars.....	47
6	OTHER STUDIES.....	47
6.1	SmCo versus NdFeB.....	47
6.1.1	Radiation Damage.....	47
6.1.1.1	Introduction.....	47
6.1.1.2	Neutron Irradiation.....	48
6.1.1.3	Proton and Heavy Ion Irradiation.....	49
6.1.1.4	Low- and Medium-Energy Electron Irradiation.....	49
6.1.1.5	Low-Energy Gamma Ray Irradiation.....	49
6.1.1.6	Low-Energy Bremsstrahlung Irradiation.....	49
6.1.1.7	Electron Beam (2 GeV) Irradiation.....	49
6.1.1.8	Future Directions.....	50
6.1.1.9	Magnet Choice.....	50
6.1.2	Magnetic Field Considerations.....	51
6.1.3	Temperature Dependence.....	52
6.1.4	Other.....	52
6.2	End Phasing.....	53
6.2.1	Remotely Adjustable End-Gaps.....	53
6.3	Fine Adjustment of Effective Magnetic Field.....	54
6.3.1	Temperature Regulation.....	54
6.3.1.1	Air Cooling/Heating.....	54
6.3.1.2	Water Cooling.....	55
6.3.1.3	Active Heating.....	55
6.3.2	Shunt.....	55
6.3.3	Canted Pole Gap.....	58
6.3.4	Mechanical Shims.....	59

7	COSTS	59
8	APPENDIX	60
8.1	Appendix A: Engineering Drawings.....	60
9	REFERENCES	63

1 Introduction

The Linac Coherent Light Source (LCLS) undulator line will consist of 33 undulator segments separated by breaks of two different lengths. The undulator segments are 3.4-m-long permanent-magnet planar hybrid devices with a period length of 30 mm and a magnetic gap of approximately 6 mm. Focusing quadrupoles, in a FODO lattice, and electron-beam diagnostics will be located in the breaks between undulator segments. Every third break will be longer in order to also accommodate x-ray diagnostics. Thus, taking the alternating focusing and defocusing quadrupoles into account, the “super-period” length before the undulator line repeats itself is six undulator segments. For additional details on the LCLS project and the undulator line, please refer to the conceptual design report (CDR).¹

A full-length prototype undulator segment has been designed, manufactured and tested, and this document provides a comprehensive report of our experience with the prototype. It contains sections on the overall design philosophy and presents many important measurements including magnetic measurements of the magnet blocks, as well as of the assembled device, and mechanical and thermal measurements. It also contains a summary section (section 5) and one section that summarizes some remaining issues being investigated (section 6).

2 Undulator Requirements

The x-ray output of the LCLS will be noisier than what synchrotron users are accustomed to, because noisiness is intrinsic to the self-amplified spontaneous emission (SASE) process. The noise level can be reduced somewhat by operating the free-electron laser (FEL) at saturation. The total length available for the undulator line is limited (although less so today than at the beginning of the project), so a goal in setting the design requirements of the undulator line was to minimize the FEL gain length, which will also minimize the total length of undulator needed to reach saturation. A tolerance budget was worked out for the parameters that affect the saturation length, assuming simultaneous worst cases for all parameters. The overall tolerances for the undulator line were then used to determine tolerances for a single undulator segment. These tolerances are: the trajectory walk-off from a straight line must not exceed 2 μm in either transverse direction; the reduction in spectral intensity of the zero-angle radiation as compared to an ideal undulator must not exceed 4%; the calculated electron phase slippage for undulator-to-undulator segment from the design value must be less than 10° ; and the undulator median plane must be well defined (and after that aligned) with an accuracy better than 50 μm vertically. These tolerances, combined, give an increase in the power gain length by 3%. (Details on how those were derived are given in section 8.2 of the CDR.)

2.1 LCLS Undulator Specifications

The undulator specifications were derived from minimization of the power gain length and hence the overall length of the undulator line to reach saturation well within 120 m from the given LCLS project parameters listed in Table 1.

Table 1. Important parameters of the LCLS project used for the undulator design.

Parameter	Specified Value
Radiation wavelength	1.5 Å
Beam energy	14.35 GeV
Normalized slice emittance	1.2 mm-mrad
Beam peak current	3.4 kA
Slice energy spread (standard deviation)	1.4 MeV

The derived and selected undulator design parameters are listed in Table 2. For this set of parameters and an optimized beta function, the saturation length was calculated to be less than 90 m.

Table 2. Undulator line design parameters.

Parameter	Specified Value
Undulator type	Planar hybrid
Magnet material	NdFeB
Pole material	Vanadium permendur
Pole gap	6 mm
Period length	30 mm
Effective magnetic field	1.325 Tesla
Effective K value	3.710
Undulator segment length ^a	3.40 m
Number of segments	33
Segment break lengths ^b	207; 441 mm
Total undulator length	112.8 m
Total line length	121.1 m

^a The length of the titanium housing (3400 mm) is used as reference.

^b The prototype undulator has 226 poles and 225 magnets per jaw, thus there is a minimum number of 113 whole periods of phase slippage per undulator segment. The segment break length of 207 mm and the length of the titanium housing of 3400 mm define the length for 113 periods of phase slippage (3.607 m).

2.2 FEL Performance-Driven Tolerances

The undulator segment tolerances derived from the physics requirement to limit the increase of the overall power gain length to 3% due to imperfections is summarized in Table 3.

Table 3. Undulator segment tolerances.

Parameter	Specified Value
Trajectory excursion (both planes)	2 μm
Radiation amplitude deviation	2%
Phase slippage between undulators	10° ^a
Vertical positioning error	50 μm

^a Total allowed phase slippage including all errors. The error in the effective magnetic field B_{eff} totally dominates the contributions.

Implicit in the phase-slippage tolerance between undulator segments is the need to maintain the magnetic field strength very precisely along the whole undulator line. It can be translated into a tolerance for the effective magnetic field (B_{eff}). An error of 1.5×10^{-4} in B_{eff} corresponds to a phase error of 10°.

2.2.1 End-Phase Compensation

It is possible to partially compensate for a variation in B_{eff} between two undulator segments by adjusting the phase slippage between them. We have investigated how effective this compensation can be and how large a deviation in B_{eff} can be compensated. Provision was made in the prototype undulator for independent adjustment of the phase slippage at either or both ends by adjusting the gap of the last seven periods with submicron resolution, as described in section 3.3.9.

We used the simulation code RON² to investigate the effect of undulator magnetic field variations on the power output at 1.5 Å. The code calculates the Fourier harmonic of the beam current density J at the frequency $2\pi c / \lambda$, where λ is the radiation wavelength (1.5 Å). The power, which is proportional to $|J|^2$, grows exponentially after the startup regime for an ideal system with no errors. This study includes a realistic electron beam with finite emittance and beam energy spread. It also includes a realistic undulator arrangement with: 1) two short breaks and one long break between the undulator segments, and 2) quadrupoles in each break to focus the beam. (The simulations used slightly larger beam emittance and beam energy than those listed in Table 1, but relative loss of gain does not depend sensitively on those parameters.)

Every element was perfectly aligned in the simulations, and the beam was matched at the entrance of the first undulator. The effective magnetic field B_{eff} was then allowed to vary from one undulator to the next using uniformly distributed random K values, i.e., $\Delta K/K (= \Delta B_{eff}/B_{eff})$ was allowed to change at random in the range $(\pm 3.5, \pm 7.0, \pm 10.5) \times 10^{-4}$. (The increment of 3.5×10^{-4} was chosen because it corresponded to a preliminary estimate of the undulator magnetic field change for 1°C temperature change, see section 4.3.3). A uniform distribution (rather than a Gaussian distribution) of errors was chosen because it limits the maximum deviation. We consider this to be more realistic because the undulator segments will be adjusted during magnetic measurements to the same B_{eff} (within 1.5×10^{-4} if end-phase compensation is not used), and after that the main contribution to the errors will be temperature variation. The undulator environment will be temperature controlled, so we anticipate that there will be a maximum deviation. The phase adjustment between the undulators was either turned off or on, and both cases are discussed below.

The calculated beam current density versus distance along the undulator line is shown in Fig. 1 for the case with no phase correction applied between the undulators (saturation will not be seen using the code RON since it is a linear code).

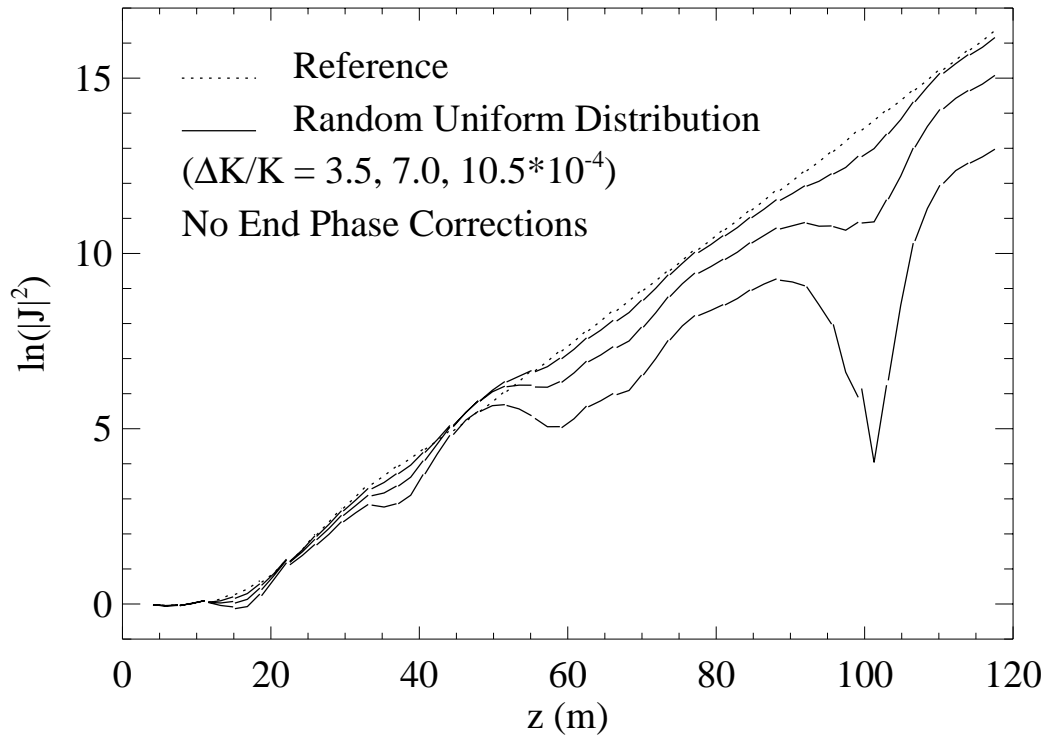


Fig. 1. Simulation of gain (log of the beam current density) for the LCLS undulator line at 1.5 \AA and 14.35 GeV with no attempt to adjust the phase between the undulators to compensate for the variation of K values. The dotted line shows the performance for ideal conditions. The broken solid lines show the expected performance for different magnitudes of $\Delta K/K$ ($3.5, 7.0, 10.5 \times 10^{-4}$, the smallest value is at the top; errors uniformly distributed at random). The curves are segmented due to the breaks between the undulators.

Although the case for $\Delta K/K = \pm 3.5 \times 10^{-4}$ appears to give an acceptable performance, the loss is too large near 100 m. (A different set of random numbers would yield a different appearance of the gain curve; wiggles of the same magnitude would occur but at different locations.)

The results with end-phase corrections applied are shown in Fig. 2. There is a dramatic improvement as expected. In fact, this was the reason that the end-gap adjustment of the phase was built into the prototype. An error of $\pm 7.0 \times 10^{-4}$ produces a negligible loss of gain in this case. The effect on gain length and saturation length for the end-gap-tuned cases are summarized in Table 4.

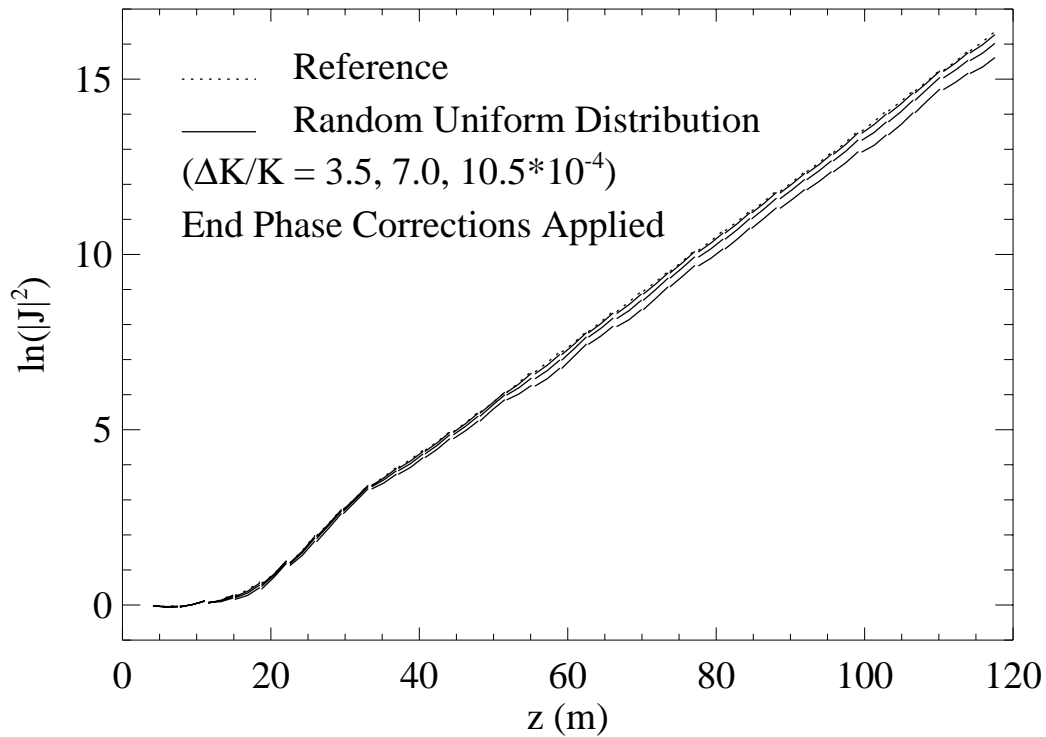


Fig. 2. Simulation of gain for the LCLS undulator line (same distribution of K values and same notation as in Fig. 1) but with optimal end-phase corrections turned on. An error of $\pm 7.0 \times 10^{-4}$ produces a negligible loss of gain.

Table 4. Calculated gain length and increase in saturation length using uniformly distributed random K values from one undulator to the next with optimal end-phase corrections applied for the LCLS beam parameters.^a

$\Delta K/K$	Gain length (m) ^b	Increase in saturation length (m) ^c
$\pm 3.5 \times 10^{-4}$	6.46 *	-
$\pm 7.0 \times 10^{-4}$	6.50	~ 1.7 m
$\pm 10.0 \times 10^{-4}$	6.60	~ 3.4 m

^a Normalized beam emittance was 1.5 mm-mrad, beam energy spread 2.1×10^{-4} , FODO lattice strength 0.112 m^{-1} , and peak current 3.5 kA. Other parameters same as in Table 1.

^b The gain length was derived over the next-to-last super period of six undulators, where the FEL process has proceeded well into the exponential gain regime.

^c The increase in saturation length was estimated near 100 m by determining how much additional distance was needed to reach the same level of $\ln(|J|^2)$.

* Same value as for $\Delta K/K = 0$.

Thus, by applying end-phase compensation to change the phase slippage between undulator segments, variations in B_{eff} up to $\sim 7 \times 10^{-4}$ will result in only minimal loss of FEL gain. This assumes that the beam properties are stable enough, and the intra-undulator diagnostics are sensitive enough, to permit tuning of the phase slippage.

3 Design and Assembly

3.1 Introduction

The overall magnetic and mechanical undulator design was driven by the main LCLS parameters summarized in Table 1 (section 2.1) and the undulator segment tolerances listed in Table 3 (section 2.2). Specifically,

- The ability to reach saturation well within the available length of 120 m was fundamental in defining the undulator magnetic field strength and determining the undulator magnetic design. A planar permanent-magnet hybrid design with quadrupole lenses located in break sections between undulator segments to provide focusing, was chosen—other designs were also investigated but rejected. Computer calculations complemented by computer simulations optimized the undulator segment length to 3.4 m, the undulator period length to 3.0 cm, and set the strength of the quadrupoles.³ The value of the undulator magnetic field strength of 1.325 Tesla (effective field on-axis; K value 3.71) determined the

nominal magnetic gap of 6.0 mm. The required magnetic field strength and magnet quality is available today in rare-earth permanent magnets due to remarkable technological advances during the past 20 years.

- The tolerance criteria given for acceptably small loss of FEL performance at 1.5 Å, most notably the undulator-to-undulator segment phase slippage (10°) and the beam trajectory walk-off ($< 2 \mu\text{m}$), and the required long-term stability were the prime factors requiring a very rigid mechanical design.
- Ease of assembly and magnetic tuning.

Initially a short model (5 all-aluminum periods) was designed and manufactured to gain experience in preparation for manufacturing of the full-length prototype undulator.⁴ In this section we present our experience with the full-length (3.4 m; 112 magnetic period long) prototype undulator.

3.2 Magnetic Design

A concern with LCLS undulators is the likelihood of loss of magnetic field strength due to radiation-induced demagnetization of the permanent-magnet blocks. The high field strength of permanent magnets is needed, but NdFeB magnet material (used in the prototype undulator) is sensitive to radiation. Demagnetization has been seen in the undulators at the European Synchrotron Radiation Facility,⁵ as well as at the Advanced Photon Source (APS),^{6,7} so it is a well-recognized risk. Resistance to radiation damage can be enhanced by the choice of magnet material and by the magnetic design of the undulator (see section 6.1.1 for a comparison of SmCo versus NdFeB).

The likelihood of radiation-induced demagnetization has been found to increase when the demagnetizing field experienced by the magnet block is stronger.⁸ Therefore, a larger margin between the demagnetizing field experienced by the magnet block and the demagnetizing field at which the block will demagnetize is expected to give a higher resistance to radiation-induced demagnetization. To get the larger margin, we: i) chose a grade of magnet material with a high coercivity, and ii) designed the magnetic structure to keep the demagnetizing field down.

The grade of magnet material chosen was N39SH from Shin-Etsu, which has a high coercivity of $\sim 1700 \text{ kA/m}$ and does not sacrifice magnetic remanence as compared to the older N38H grade, which has been used in many insertion devices, including most of those at the APS. During the magnetic design process, the localized demagnetizing field experienced by different parts of the magnet blocks was examined over the full range of gap possibilities. A goal in the design was to maximize the on-axis field of the undulator while ensuring that the demagnetizing field seen by the magnets is not excessive at the chosen device gap. The magnetic design model for the prototype undulator magnetic structure is shown in Fig. 3 (see section 8.5 of the CDR for additional details.)

Straightness of the trajectory is a significant requirement for the undulators, and a proper design for the ends of the undulators will help keep the trajectory straight. The strengths of the poles at the ends of the undulators will go in the sequence 0.25, 0.75, 1. This gives an entrance into (and exit from) the undulator that has no angular kick and no trajectory offset.

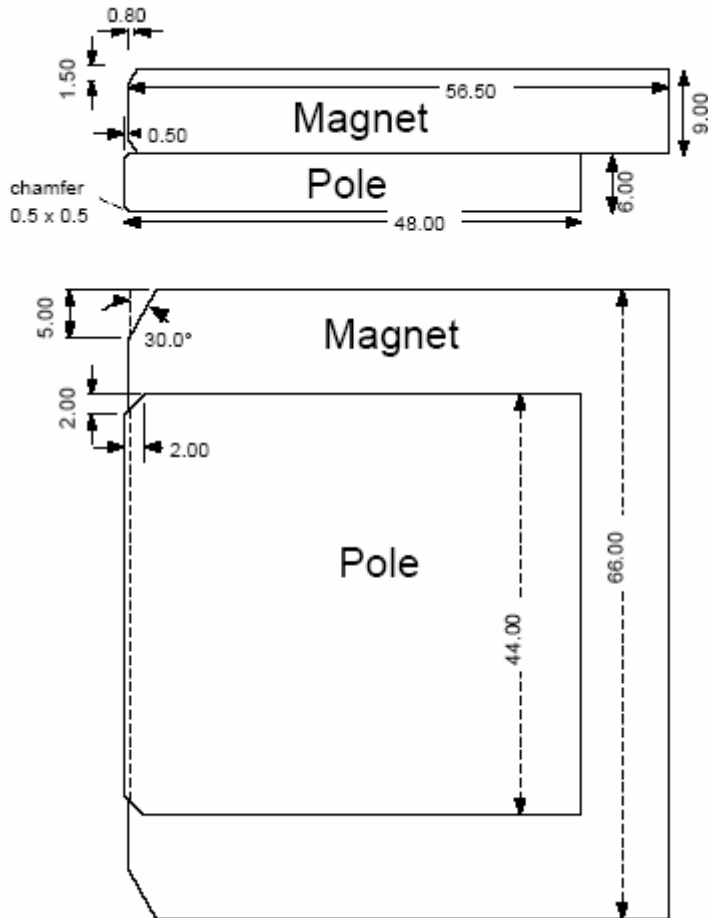


Fig. 3. Magnetic design for the prototype undulator magnetic structure. From the CDR¹ (dimensions in mm).

3.3 Mechanical Design

This section gives a detailed description of the main mechanical components of the prototype undulator (see also section 8.6 in the CDR). For some components, the initial design was modified, e.g., clamping of poles, and such changes are explicitly spelled out using the notation “revised prototype” or the “production undulator.”

3.3.1 Requirements

In the beginning, two basic design considerations were discussed: i) to use a C-shape design or O-shape design of the housing that holds the magnets and poles, and ii) to use a fixed-gap or a variable-gap undulator.

A C-shaped housing was favored over an O-shaped form (although there is a small asymmetry when deformation due to gravity and magnetic forces is considered) because there is open access to the magnetic structure for tuning and magnetic measurements and for inserting the vacuum chamber. A variable-gap undulator was ruled out because of the tight mechanical tolerances. Further, a fixed-gap undulator is cheaper, generally more rigid, and simpler to design. The assembly of the magnets and poles in the housing must be simple and fast (yet highly precise), and provision for simple magnetic tuning must be built into the design. Built-in (partial) thermal compensation of the B_{eff} is also desirable. The prototype undulator meets all these criteria.⁹

3.3.2 Mechanical Tolerances

Based on the undulator segment tolerances, the prototype undulator was designed using the mechanical tolerances listed in Table 5.

Table 5. Prototype undulator design mechanical tolerance specifications.

Parameter	Tolerance
Pole-gap tolerance	± 0.006 mm
Neighbor pole-gap difference (selective assembly)	± 0.003 mm
Period variations: between neighboring poles	± 0.050 mm
accumulated error	± 0.050 mm
Pole thickness	-0.05 mm
Pole transverse displacement (top and bottom)	± 0.20 mm
Pole displacement in longitudinal (z) direction (top and bottom)	± 0.10 mm
Pole-face parallelism: top and bottom	< 0.1 mm
angle may open outside only	< 1.75 mrad
Pole-gap rotation around “z” axis over the whole length	< 5.25 mrad
Undulator segment sag due to its weight in the vertical (y) direction	< 0.002 mm
Undulator gap adjustment: possible	± 0.005 mm
adjustment resolution	0.001 mm

3.3.3 Design Features

Several of the main design features of the prototype undulator can be identified in Fig. 4, which shows the prototype undulator on the magnetic measuring stand. The housing is open on one side (so-called C-shape design) for ease of magnetic measurements and tuning, and for ease of installation of the undulator onto the undulator line without breaking vacuum. It is a fixed-gap, planar permanent-magnet hybrid device. Steel shims can be seen inserted between the aluminum base plate and the solid housing (made of titanium) at the top and bottom jaws. (They are used for coarse adjustment of the gap or K value.) Four pairs of pole side shims are also seen on the side near the poles (used to make local field adjustments for changing the trajectory).

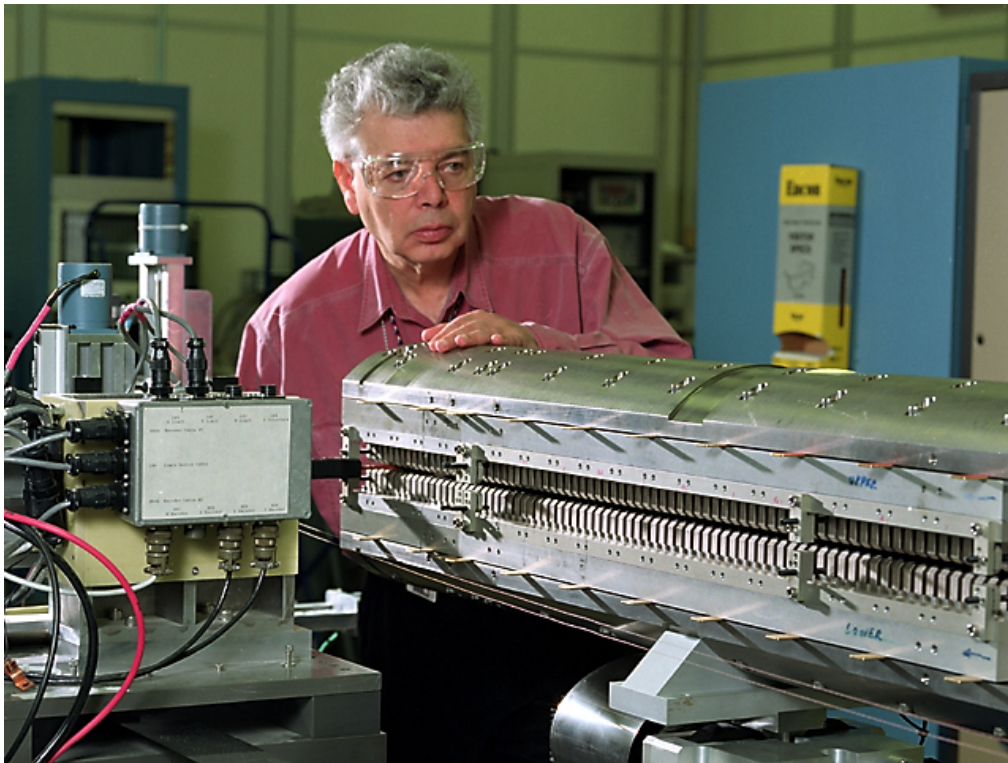


Fig. 4. The prototype undulator on the magnetic measuring stand (the full length is not shown). It is a fixed-gap, planar permanent-magnet hybrid device in an open C-shape design with the housing made of titanium. The permanent magnets, which are larger than the poles, are seen protruding in the upper and lower jaws (poles cannot be seen). Four pairs of pole side shims (trajectory shims) for local field tuning and steel shims between the aluminum base plate and the titanium housing for gap adjustment are clearly seen in this photograph. An ample number of pole side shims can be attached onto the aluminum side racks, which have pre-drilled holes for positioning the shims. The piezoelectric translators (for fine adjustment of the end gaps) were not installed when this picture was taken. The magnetic pole gap is 6.35 mm.

The complete list of major design features is summarized here and described in more detail in the sections that follow:

- The titanium housing is made from a forged 12" bar and machined into the final so-called C-shaped form.
- The pole and magnet base plates are made of aluminum alloy to partially compensate for the temperature dependence of the permanent-magnet remanence field by changing the pole gap with temperature (as the temperature rises and the magnets lose strength, the differential thermal expansion between the aluminum base plate, the vanadium permendur poles and the titanium housing results in the gap closing slightly).
- The poles are made of vanadium permendur with so-called "wings" made of titanium. The wings fit into the grooved side racks and are also used to clamp the poles in place (for the revised prototype).
- Only one clamp was initially used for each pole and magnet. In the revised prototype, two clamps are used for each pole. The clamps are made of titanium. Magnets are still clamped on one side only. The magnetic forces do not tend to move them out of their locations once they are fully inserted into the grooved base plates. This is not true for the poles.
- Incremental shims and "push-pull" screws were initially used for the undulator gap adjustment. For the revised prototype, only the "pull" screws are used to "pull" the jaws tight towards the titanium housing. The actual gap is then determined by the thickness of the steel shims that are placed between the aluminum base plates and the titanium housing.
- Piezoelectric translators are used to precisely tune the magnetic field strength at both ends of the undulator (two on each end; one each on the top and bottom jaws). They can be remotely adjusted and will be used to phase tune one undulator segment to the next to maximize the FEL gain.
- One side is completely open for side-shim installation in order to tune the field strength locally, where necessary, along the length of the undulator segment. Also, this design allows for easy access and precise magnetic measurements.
- The pole side shims initially had six bars made of low-carbon steel, which were reduced to four in the revised prototype. Each bar can be individually adjusted and locked in place.
- Five camshaft movers are used for horizontal and vertical alignment of the undulator as a whole.

The cross section of the prototype undulator is shown in Fig. 5. The design was subsequently changed to include two clamps per pole instead of one (revised prototype)—see section 3.3.7 for more details.

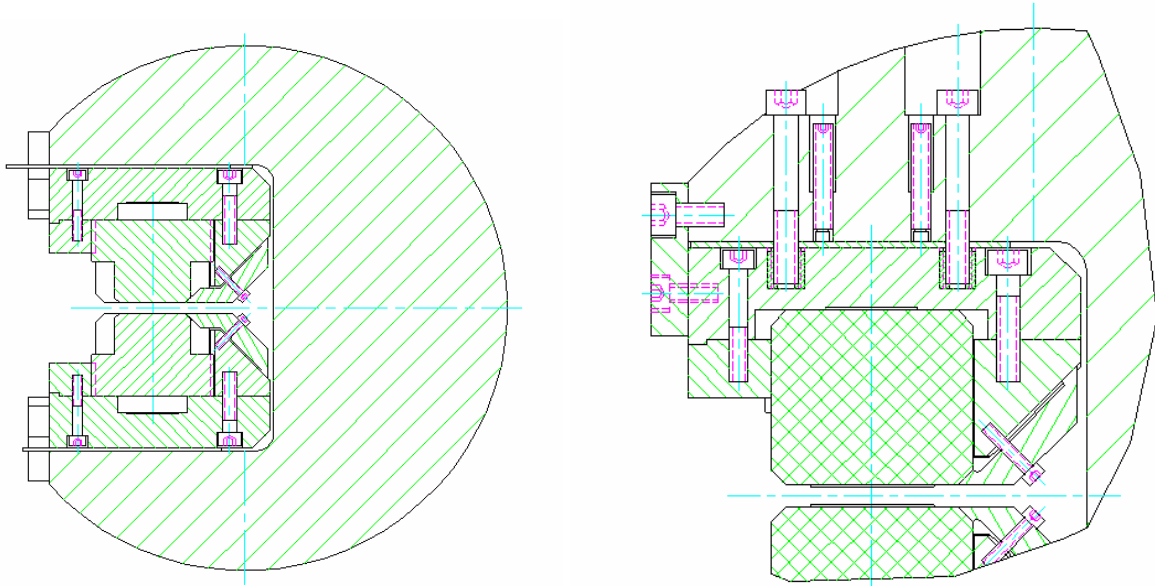


Fig. 5. Cross section of the prototype undulator before clamping of the poles was changed. Left: cross section through the poles with one clamp holding the poles. This design was subsequently changed to use two clamps per pole. The magnets can be seen extending beyond the poles transversely except near the non-magnetic wings near the base. Right: cross section through the magnets. One clamp is sufficient to hold the magnets because the magnetic forces push the magnets away from the gap and into the base plate. The “push-pull” screws for setting the gap are also seen (the “push” screws have been eliminated for the production undulator. They are not used in the prototype undulator. The magnets are positioned in the grooves of the base plate making them extend beyond the poles (in the direction away from the gap). The poles are placed on top of the ridges of the base plate and are positioned with the help of narrow grooves in the two side racks (the rectangular and triangular shaped cross sections shown on the left). This design provides for a fast and accurate assembly of the magnetic structure.

3.3.4 Choice of Housing Material

Choices for the housing material are limited keeping in mind that this material must be non-magnetic. In fact, the practical choices are limited to stainless steel, brass or bronze, aluminum alloy and titanium alloy. Below we list the main advantages and disadvantages for each of the materials investigated. A series of finite element analyses of the choice of material was also performed to ensure that the overall best choice was made.¹⁰

Stainless Steel

Stainless steel of the size needed for the housing might be slightly magnetic from the very beginning. Also austenitic stainless steel may become magnetic due to

transformation from austenite to martensite during cold work and even during machining, if it is heavily deformed. A corrective anneal may be necessary if a low magnetic permeability is required. Precise machining is difficult (in general, more specific to the austenitic stainless steels). Also stainless steel is not the best material for long-term dimensional stability, particularly for nonsymmetrical machining, which is the case here.

Advantages: Commercially available, relatively cheap.

Disadvantages: High density, large coefficient of thermal expansion, might become magnetic during machining, difficult to machine to very high precision, requires a minimum of a two-step stress-relief process, not a good material from a long-term dimensional stability point of view.¹¹

Brass and Bronze

Advantages: Commercially available, relatively cheap, easy to manufacture.

Disadvantages: High density, soft, low Young's modulus, large coefficient of thermal expansion, very questionable long-term dimensional stability.

Aluminum Alloys

Advantages: Commercially available, cheap, low density, easy to manufacture.

Disadvantages: Soft, the highest coefficient of thermal expansion, impossible to use heat treatment for relieving stress (material will lose temper), low Young's modulus.

Cast Aluminum Alloys

Advantages: Possibility to decrease the amount of machining to avoid heat treatment for relieving stress.

Disadvantages: Rather expensive, requires special tooling, structural integrity is questionable due to possibility of voids.

Titanium Alloys (6Al-4V)

Disadvantages: Expensive.

Advantages: Commercially available, low density, rigid, high Young's modulus, small coefficient of thermal expansion, easy to machine, one-step stress relief, the best long-term dimensional stability.

Based on the small thermal expansion, the low density, the high rigidity, the long-term stability, and the ease of machining, the Ti alloy 6Al-4V was chosen for the prototype undulator.

3.3.5 Base Plate (Six Piece)

The machined precision of the aluminum base plates (specified flatness tolerance of 50 μm) and the precision of their attachments to the housing are very important because the pole gaps depend directly on those, which in turn affects the magnetic field uniformity in the gap-center of the undulator and hence the beam trajectory. The base plates (along with the side racks and clamps) hold the pole and magnet assembly together. The poles and magnets are clamped from the side to keep them in the correct positions so that they do not move due to the strong magnetic forces present (see Fig. 5 in

section 3.3.3 and Fig. 7 in section 3.3.7). The base plate is divided into three ~ 1-m-long central pieces per jaw (six per undulator) to simplify the assembly process (see section 3.4.2) and two ~ 20-cm-long end pieces per jaw (four per undulator) to provide for the necessary undulator-to-undulator phase tuning by changing the end gaps with piezoelectric translators (see section 3.3.9).

The base plates are made of aluminum alloy so that the undulator gap will close with increased temperature (and open if the temperature decreases) for the purpose of compensating for loss (increase) of remanence magnetic field. The compensation relies on the difference in thermal expansion between the base plate (aluminum alloy), the vanadium permendur poles, and the titanium housing, and one achieves a partial compensation for the loss of remanence with increased temperature (see section 4.3.3).

3.3.6 Poles (with “Wings”)

The poles are made of vanadium permendur. The magnetic design for the undulator was shown in Fig. 3. As can be seen, the magnets overlap the poles on three sides (both in the width and in the height away from the gap), and, for such a design, it is difficult to clamp the poles so that they are accurately positioned in the longitudinal direction. In some designs, a wedge is added to the bottom of the pole and to the base plate that holds the pole.

Instead we have attached so called “wings” made of titanium to each side of the poles, see Fig. 6. (Titanium was chosen because it is nonmagnetic, and the coefficient of thermal expansion matches closely that of vanadium permendur.)

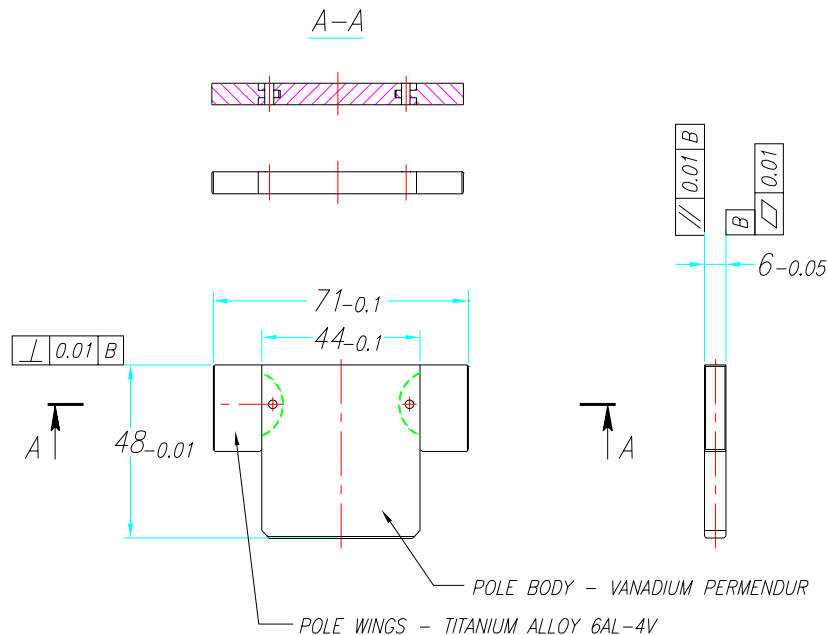


Fig. 6. Prototype undulator pole design (dimensions in mm). Titanium “wings” are attached to the vanadium permendur poles.

The final grinding of the poles was done together with the wings so that the wings and the pole piece have exactly the same thickness. A final heat treatment was performed to optimize the magnetic performance. The wings of the poles extend beyond the magnets, and the poles can therefore easily be placed in the two grooved side racks during assembly of the magnetic structure. Side clamps, made of titanium, are used to secure the poles.

3.3.7 Clamps

The initial intention was to use only one clamp per pole and magnet. One of the design goals was to keep one side of the undulator completely open to have easy access to the pole gap during magnetic measurements and to provide as much space as possible for the pole side shims. However, using only one clamp for the poles proved not to be the best choice. With only one clamp, the poles rotated slightly when subjected to the full magnetic force, thereby reducing the gap and creating cant. In an attempt to prevent this rotation, the clamping force was increased; however, this led to bending of the aluminum base plate. A decision was made to modify the design to use two clamps—one on each side of the pole (see Fig. 7). Only one clamp is still used to hold the magnets due to the fact that the magnetic forces push the magnets away from the gap, and the tolerance for the magnet position is not very tight. Due to the added clamps for the poles (on the outboard side), it was necessary to reduce the number of bars in the pole side shims to four (from six)—see section 3.3.10.1. There were no other implications due to this change, which was easy to implement in the current design, and there is still easy access to the gap for placing shims and making measurements.

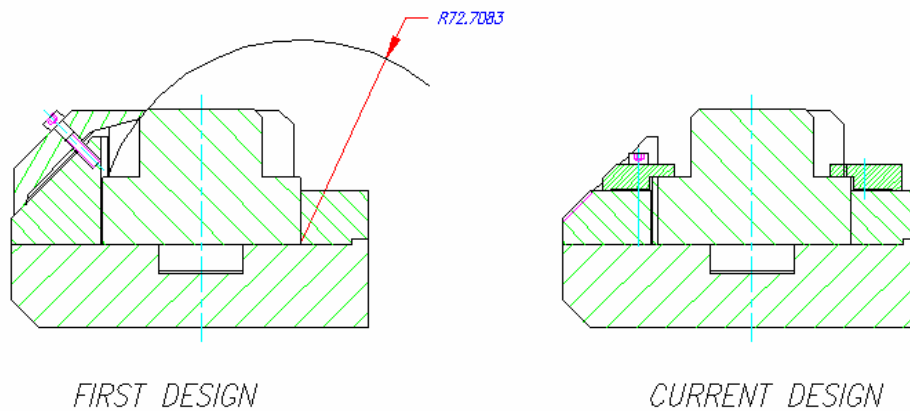


Fig. 7. Cross section through poles. Left: the initial design with only one clamp per pole. Right: the current design of the prototype with two pole clamps per pole. The outboard side (the open side of the ‘C’) of the undulator is on the right side in each case.

3.3.8 “Push-Pull” Screws and Incremental Shims for Gap Adjustment

“Push-pull” screws (Fig. 5) were included in the design of the prototype undulator to provide a means of accurately adjusting the undulator gap or K value. However, while working with the prototype, it was found that the “push-pull” screws were complicated to use and were not the best choice for adjusting the gap to the precision needed. So it was decided to use only the “pull” screws in combination with added low-carbon steel shims placed between the base plate and the housing. This change was made possible because the titanium housing had been machined with a $50\ \mu\text{m}$ precision over its entire length (3.4 meter)—a value obtained using thermal stress relief after the rough machining.

Initially shims were made of brass; however, magnetic measurements have shown that small (up to 2-mm-thick) low-carbon steel shims have no impact on the undulator magnetic performance. Thus, the actual gap will be determined by the thickness of the selected shims that can be made with a very high incremental accuracy (tolerance of $\sim \pm 2.5\ \mu\text{m}$ has been achieved, see section 6.3.4), and the tightening of the “pull” screws.

3.3.9 Remotely Adjustable End-Gaps

The two end sections of the magnetic structure (each about 20 cm long) were designed so that they can be bent by remotely controlled piezoelectric translators. There are two piezoelectric translators at each end—one on the top jaw and one on the bottom jaw. They are placed in holes made in the undulator housing, and each of them has a travel range of about $100\ \mu\text{m}$ (for a maximum gap change of about $200\ \mu\text{m}$)—see Fig. 8.

Push and pull forces directed to the base plate cause the gap to change. This design was thoroughly checked during the magnetic tuning and testing of the prototype, and it was found to work well. (The results of the piezoelectric translator tests are further described in section 4.3.6). Nevertheless, because of the ongoing design changes to improve the method for setting the desired effective magnetic field, the piezoelectric translators and the variable end-gaps may become obsolete for the production undulator (see section 6.2 for further discussions).

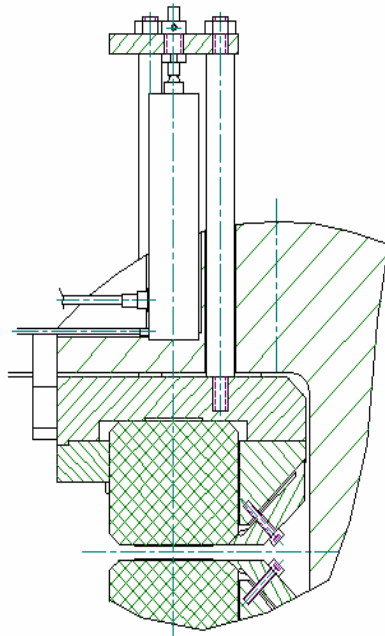


Fig. 8. A cross section of one piezoelectric translator at one end section (top jaw only). It shows the translator in the center of the figure with one of the rods attached to the base plate. Push and pull forces directed to the base plate cause it to bend. The plate is segmented, and the section that bends is about 20 cm long. (A small bend of maximum 100 μm per plate or 200 μm per end-gap can be achieved this way.)

3.3.10 Pole Side and Phase Shims

The tolerance criterion for the trajectory excursions ($\pm 2 \mu\text{m}$ for both transverse planes) is very demanding. To reduce trajectory offsets and kicks, magnetic tuning is done using novel pole side shims specifically developed for small fixed-gap undulators. To improve phase errors, phase shims are applied on the surfaces of the magnets. Fig. 9 shows examples of both types of shims before they were installed in the undulator. Further description of these shims is given in section 8.6.2 of the CDR.



Fig. 9. Close-up view of a novel pole side shim specifically developed for small fixed-gap undulators and two regular phase shims that are placed on surfaces of the magnets. The pole side shim can use one or two threaded low-carbon steel bars (in this photograph only one bar is used).

3.3.10.1 Bar Pole Side Shims (Trajectory Shims)

Initially, each pole side shim consisted of an aluminum holder with three adjustable threaded bars (rods) made of low-carbon steel (see Fig. 10) and a locking mechanism for the bars so that they cannot move once tightened. The shims can be installed along the undulator near any pole where it may be necessary to locally adjust the magnetic field. Usually they are installed symmetrically, i.e., at both upper and lower jaws as shown in Fig. 11. The magnetic field changes significantly only near the pole where the shims are located, thus giving the trajectory a kick near this pole.

Magnetic measurements showed that the local peak magnetic field changed by as much as 5% when all six bars were used over their full range (three bars for each shim placed symmetrically at the upper and lower jaw). The initial design with three bars per shim was subsequently reduced to two per shim to make room for a second pole clamp, which was deemed necessary to avoid the pole rotation as discussed in section 3.3.7. This modification still provides for sufficient peak magnetic field adjustment ($> 3\%$).

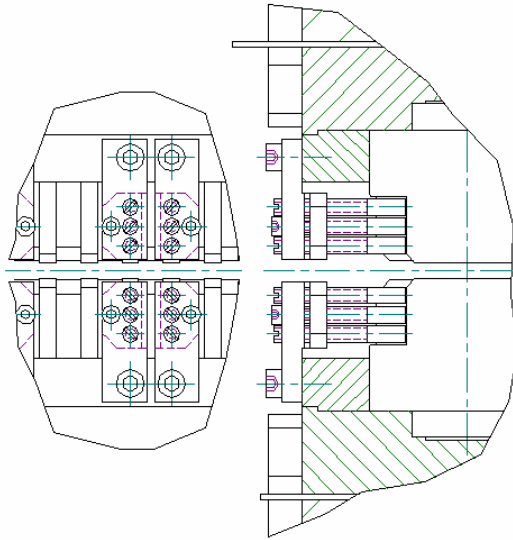


Fig. 10. Example of four pole side shims (each with three low-carbon threaded steel bars) placed symmetrically at the upper and lower jaws of the magnetic structure at adjacent poles. In the initial design (shown here), three low-carbon steel bars were used for each shim. For the revised prototype, a maximum of two bars per shim are used instead to make room for a second pole clamp (not shown). (Two bars per shim provide sufficient magnetic field adjustments.)



Fig. 11. Close-up photograph of the prototype undulator, which shows six pole side shims with one low-carbon threaded steel bar each, placed symmetrically at the upper and lower magnetic arrays. (Two bars per shim may be used to locally change the peak magnetic field up to about 3%.)

3.3.10.2 Phase Shims

To improve the phase errors and hence the spontaneous radiation amplitude, thin iron shims were made that were applied to the surfaces of the magnets. These shims decrease the peak magnetic field of two neighboring poles, hence changing the phase slippage between the electron and the radiated light, thereby providing a mechanism for tuning the phases locally. Examples of phase shims are shown in Fig. 9.

3.3.10.3 Pole Side Shims (for Horizontal Magnetic Field)

Due to the small gap (strong vertical magnetic field), the bar pole side shims (section 3.3.10.1) have little effect on the horizontal magnetic field component. Another type of shim, consisting of large solid iron plates with a width equal to that of the pole and attached to the pole side, was used for horizontal field tuning. These shims are used in pairs. The shim in the lower jaw is shifted by half period with respect to the shim in the upper jaw to cancel the vertical field disturbance and to create only a horizontal field component.

3.3.11 Magnetic Shields

The fringe fields from the termination of the undulator create an uncertainty in the tuning due to the presence of magnetic material in near proximity to the ends, e.g., components in the break sections between undulator segments. To limit the extent of this field, magnetic shields (made of low-carbon steel) were installed on the ends of the housing. Magnetic measurements of the prototype undulator showed that the initial location of the shields (attached directly to the housing) was too close to the end poles and thereby influenced the first and second field integrals due to almost zeroing the strength of the last pole. To correct for this distortion, the shields were placed 19 mm away from the housing, as shown in Fig. 12.

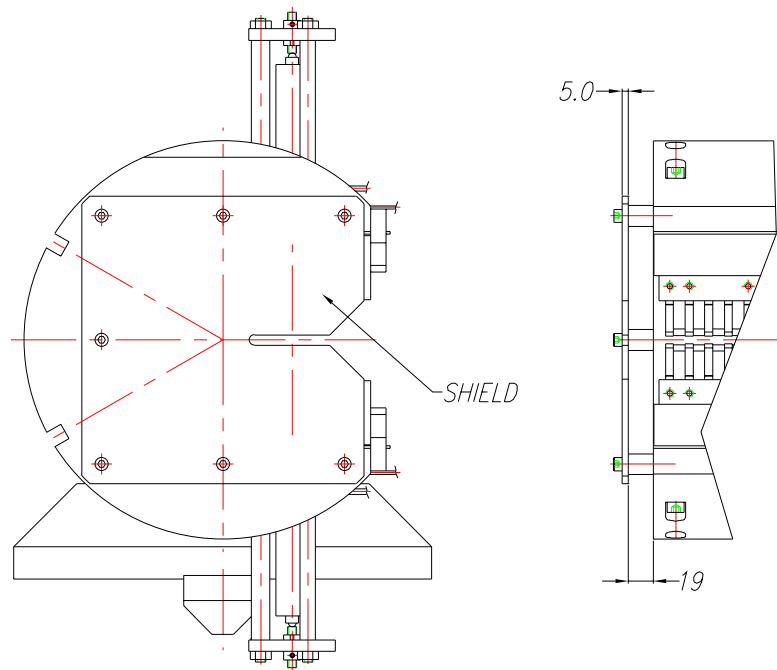


Fig. 12. Right: magnetic shield of low-carbon steel (5 mm thick) placed 19 mm from the end of the undulator housing. Left: end view of the undulator showing the shield.

3.3.12 Cam Shaft Movers for Undulator Alignment

Cam shaft movers are used for horizontal and vertical positioning of the undulator segments. Each undulator segment needs to be aligned to better than $50\ \mu\text{m}$ in the vertical direction and $100\ \mu\text{m}$ in the horizontal direction. A schematic view of the cam shaft movers is shown in Fig. 13, and the components of a mover are shown in Fig. 14. The movers are similar to the girder movers used at the Swiss Light Source. A picture of the prototype undulator on its movers and next to the 6-m-long granite bench is shown in Fig. 15.

To make the movers self-aligning, a double-row spherical ball bearing was installed on each cam shaft. During the self-aligning procedure the ball bearing “travels” slightly causing a movement jitter (see Fig. 16). However, even with this jitter, an undulator positioning accuracy of better than $10\ \mu\text{m}$ has been achieved in the vertical direction—significantly better than the required $50\ \mu\text{m}$.

During tests, we discovered that it was advantageous to use a wire potentiometer on each shaft to locate the “zero” or home position.¹² Such potentiometers were successfully installed and tested and will be properly integrated into the final design.

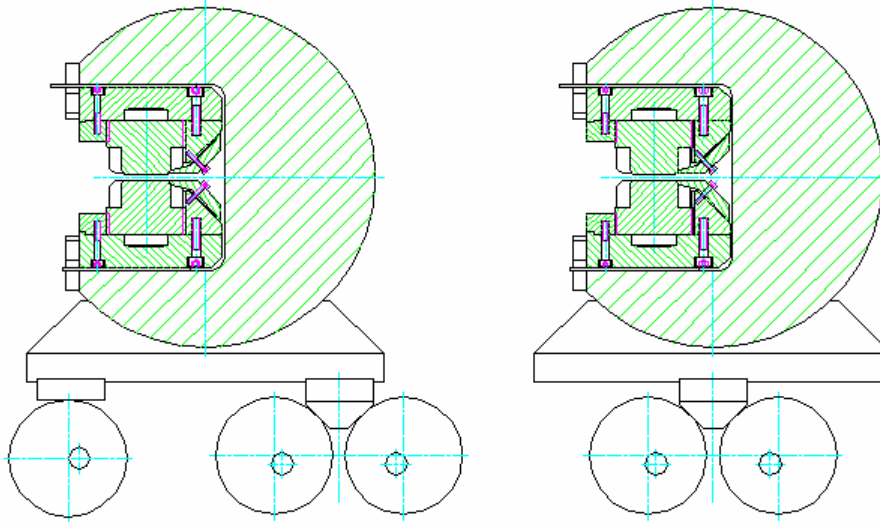


Fig. 13. Schematic of the three cam-shaft undulator positioning stages. Each cam shaft produces a reciprocating motion with a range of ± 3 mm.



Fig. 14. Cam shaft mover. Right: an end view from the motor side. Left: a top view (top figure) and a cross section of the self-aligning spherical ball bearing (bottom figure). Each mover consists of a servomotor with an integrated brake, an incremental rotary encoder, a gear box (ratio 100:1), and the self-aligning spherical ball bearing.

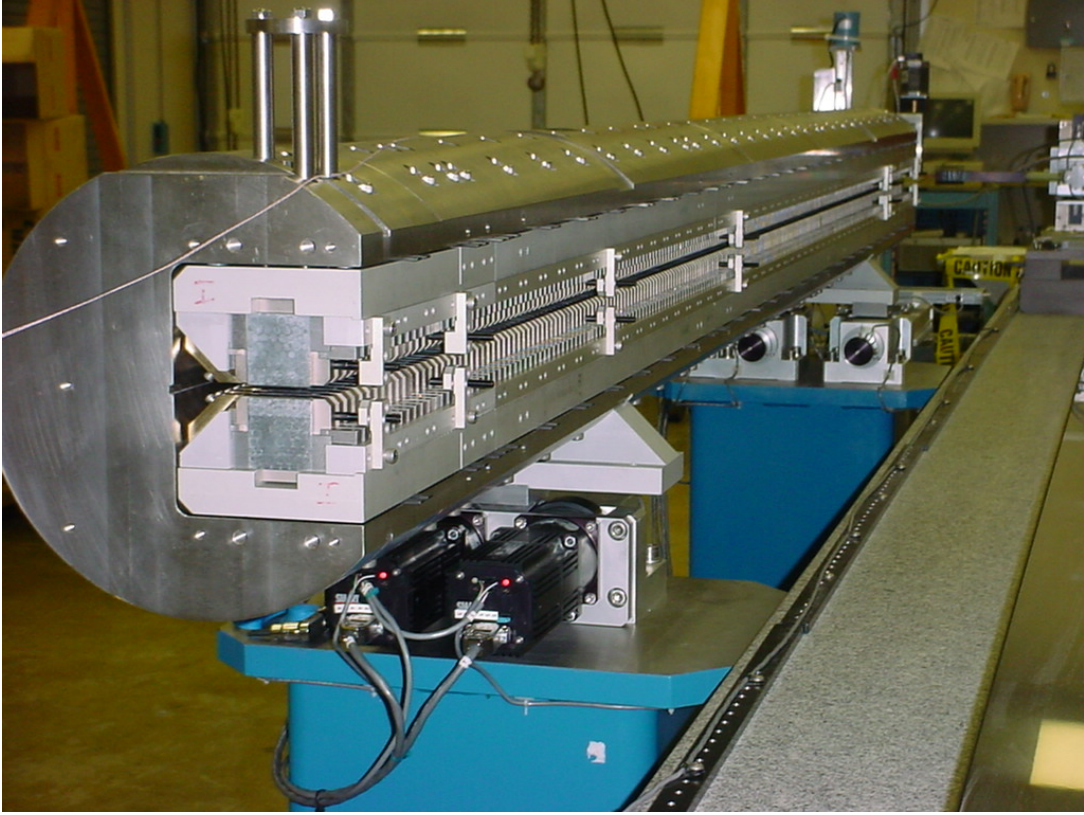


Fig. 15. Photograph of the prototype undulator positioned on the cam-shaft positioning stages next to the 6-m-long granite bench in the magnet measurement facility at the APS. The magnetic shield for the end of the undulator housing was not installed when this picture was taken.

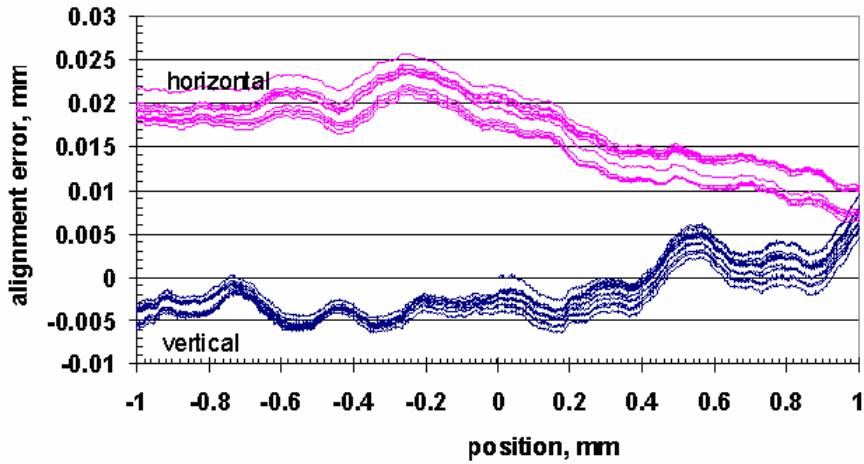


Fig. 16. Alignment errors of one cam-shaft mover measured with a high-resolution linear encoder. The figure shows multiple traces because of the slow self-alignment of the spherical bearings. The alignment error is about 10 μm and 15 μm in the vertical and horizontal directions, respectively.

3.4 Assembly of Magnetic Structure

Both magnets and poles were sorted before being assembled into the magnetic arrays. For the magnets, we relied on both the vendor's supplied data and our own measurements, and, for the poles, we used measured pole heights for the sorting. Both procedures are described in detail below.

3.4.1 Sorting

3.4.1.1 Magnet Blocks

A batch of 500 magnets with measured magnetic moments was purchased from Shin-Etsu Chemical Co. We measured approximately 10% of the magnets using a Helmholtz coil system to check the vendor's data of the magnetic moments. We found excellent agreement between our measurements and the vendor's data, and therefore we did not measure all of the remaining magnet blocks. Fig. 17 shows the distribution of the total magnetic moment of the numbered magnets as supplied and measured by the vendor.

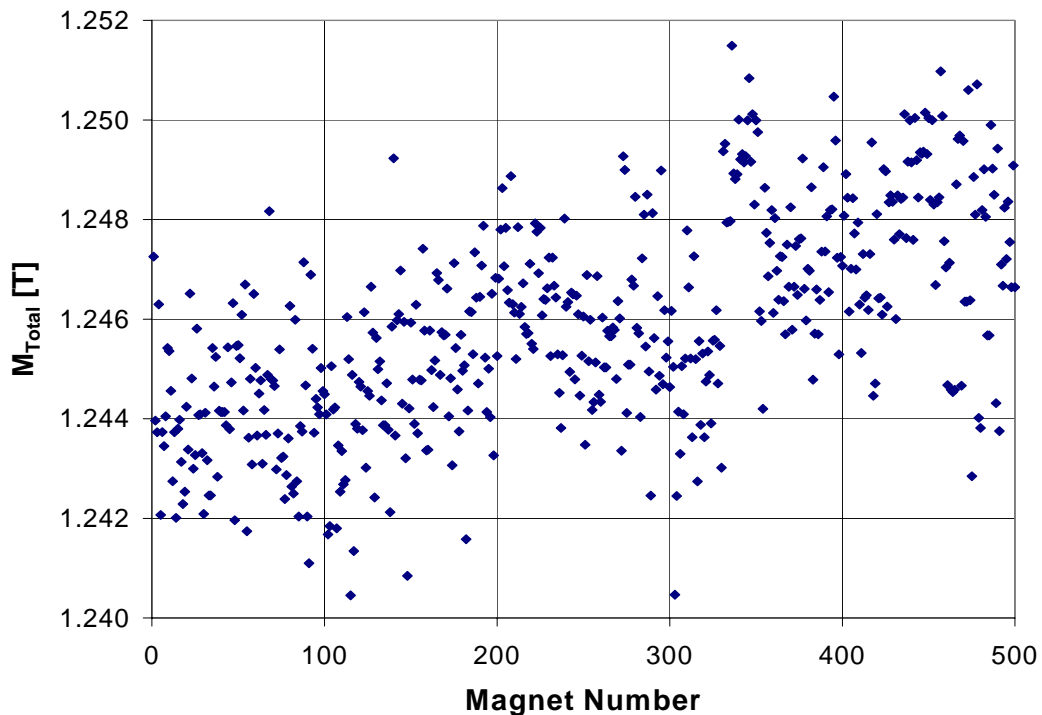


Fig. 17. Total magnetic moment of 500 magnet blocks delivered and measured by Shin-Etsu. The average is 1.246 Tesla, and the rms deviation is 0.17%.

A simple two-step sorting process was applied to the magnet blocks before they were installed in the magnetic arrays. First, the magnets for the upper jaw were paired with magnets for the lower jaw, pairing the strongest with the weakest, the next strongest with the next weakest, etc., to average out the variation. This worked extremely well because the measured magnetic moments were symmetric with respect to the average magnetization. The sorted distributions of the total magnetic moments are shown in Fig. 18.

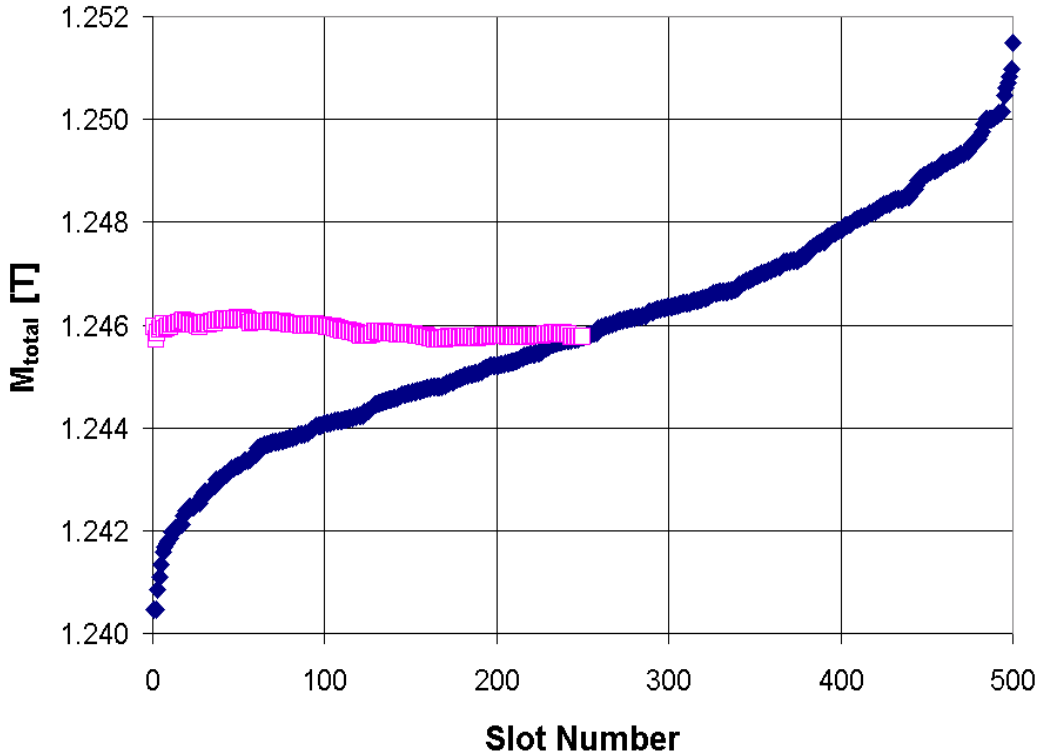


Fig. 18. Distribution of the total magnetic moment after sorting from low-to-high moments (solid diamonds). The distribution near the average is the result of pairing magnets with low and high moments (open squares). As a result, the rms deviation was reduced to 0.01%.

In the second step of sorting, we used measured field integrals of the individual magnet blocks, which were derived from Hall probe measurements of each magnet mounted in a specially designed half-period fixture with vanadium permendur poles at a pole gap of 6.0 mm.¹³ (The original design of the fixture was modified to ensure better rigidity and reproducibility, however.) The vertical component of the magnetic moment produces a vertical magnetic field in the region where the magnet is located (see section 8.4.2 of the CDR), and we measured a dependency (on average) of the first field integral (and the phase slippage) on the sign of this moment, which can point either “up” or “down” with respect to the reference magnet.¹⁴ However, the effects of a specific orientation of the vertical component were very small and could therefore be ignored.

We used, however, the value of the first field integral of the magnet blocks to estimate the second field integral of the assembled device. Although this overestimates the distortion, it is useful but not crucial. We swapped pairs of magnets with large values of the second field integral. The results before and after sorting are shown in Fig. 19. The magnetic measurements of the assembled prototype are described in section 4.3.

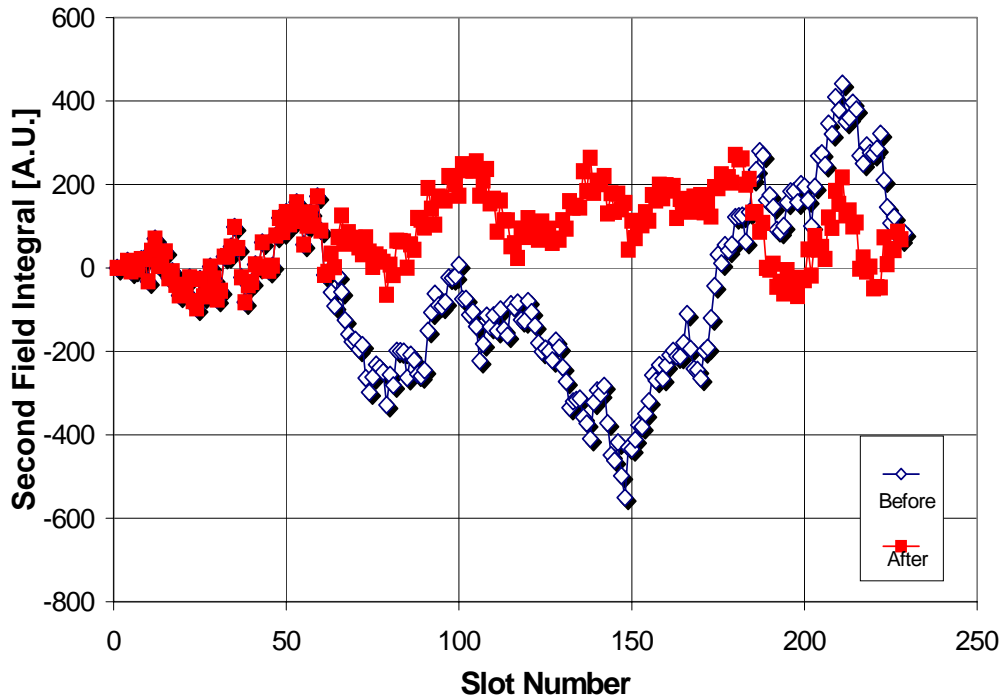


Fig. 19. Estimated second field integral along the undulator axis before swapping magnet pairs (open diamonds) and after swapping magnet pairs (solid squares).

3.4.1.2 Poles

The magnet blocks were sorted to produce very small peak magnetic field variations. As a result, the mechanical tolerance of the pole heights became a significant contributor to field-strength variations. The manufacturing specification (48.0 mm -10 μm) was deemed inadequate, and a selective assembly procedure, to pair short and tall poles, was implemented to decrease the influence of pole-gap variation on the field. Each pole height was measured at three locations (near both edges and in the middle), and short and tall poles were paired based on the measured height in the middle. The sorted measured pole-gap deviations from the average value are shown in Fig. 20. (The rms pole-gap deviation was 2.4 μm after pairing and 6.3 μm before pairing.) Also, since the poles were measured near both edges, we used this information to install a small outboard cant to allow for accurate measurement of the pole gaps ($\pm 1 \mu\text{m}$). This is illustrated and explained in Fig. 21.

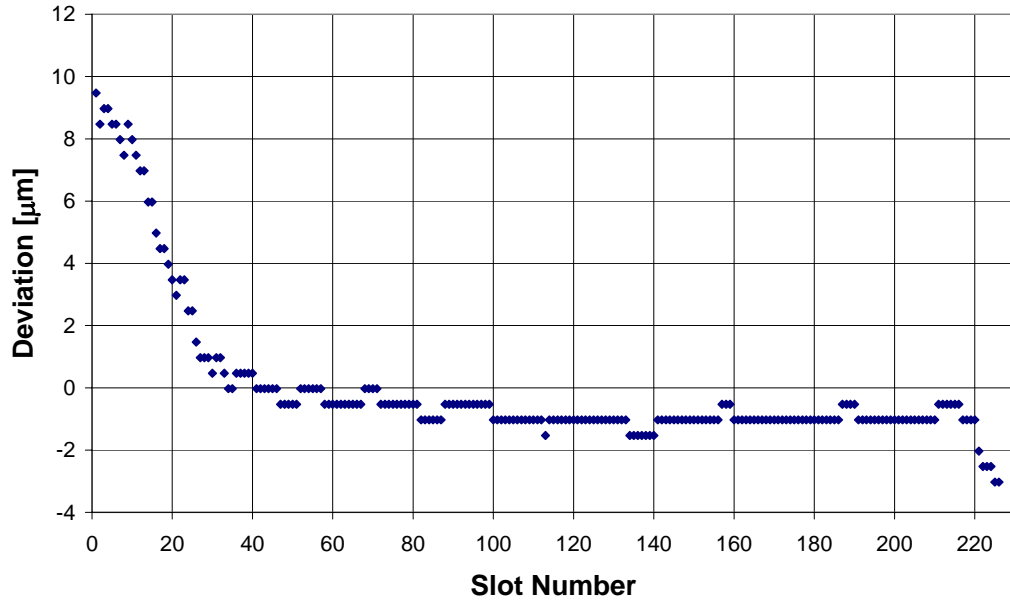


Fig. 20. Sorted measured pole-gap deviations from the average value in the middle of the poles after pairing short and tall poles. The nominal pole height is 48.0 mm (-10 μm). The rms pole-gap deviation is 2.4 μm after pairing and 6.3 μm before pairing. The slot number indicates the order in which the poles were installed in the magnetic structure.

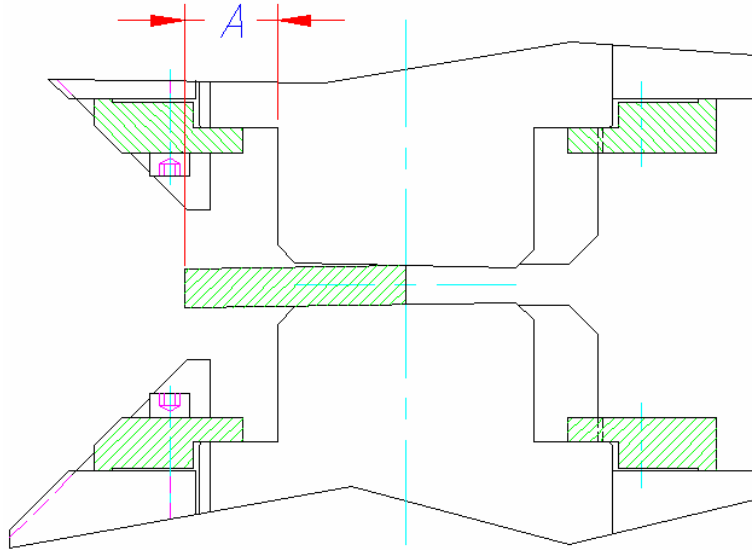


Fig. 21. Accurate measurement of the pole gap. Precise gauge blocks are used to measure the actual pole gap. The pole gap is measured by changing the thickness of the gauge block so that the measured distance “A” is kept constant. Such a technique improves the precision by at least a factor of five, and the measured pole gaps are accurate to about $\pm 1 \mu\text{m}$. The selective assembly procedure was used to create a small pole cant.

3.4.2 Assembly Process

The magnets and poles (poles first) are installed in the six ~ 1-m-long base plates (with side racks for positioning the magnets and poles, and clamps for keeping them in precise locations) before each base plate is inserted and accurately positioned in the undulator housing. A special jig was designed for this purpose, and it is described next.

3.4.3 Special Jig

The special fixture used to assemble the top and bottom halves of the magnetic structure proved to be very well designed (see Fig. 22). It allows for easy and convenient relative alignment of the top and bottom sections of the magnetic structure in both vertical and longitudinal directions while keeping them separated by an aluminum spacer. The two halves are allowed to close smoothly by using special screws from both sides, until they are only held apart by the aluminum spacer (thickness 5 mm; nominal pole-gap size is 6 mm). The attractive magnetic force, which is about 20000 N per 1-m-long section, holds the two halves tightly together. They are inserted as a single unit into the undulator housing and attached to the housing using the “pull” screws. The last step is to remove the temporary aluminum spacer.

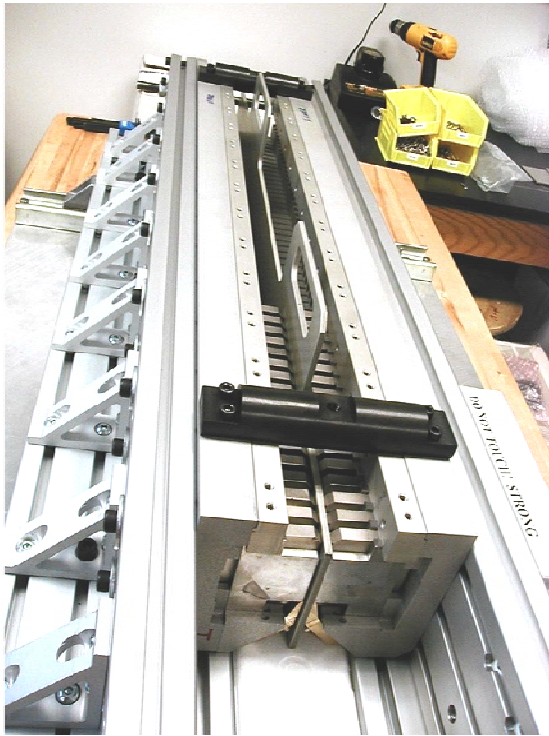


Fig. 22. Special fixture for installation and alignment of the ~ 1-m-long magnetic structures in the undulator housing. The two halves are separated by a 5-mm-thick aluminum spacer. The halves are held together by the strong attractive magnetic forces (~ 20000 N per 1-m-long section).

4 Tuning and Measurements

4.1 Introduction

The tuning and magnetic measurements of the prototype undulator are quite different compared to those of the standard undulator A at the APS due to the very different requirements and the different mechanical designs. In some regards the prototype is much simpler to tune than the undulator A. For example, it is a fixed-gap device, i.e., there is no gap dependence on the tolerances except for a slight dependency on the end-gaps that may open and close by $\pm 100 \mu\text{m}$. There are no requirements on the integrated multipole moments, and there are no requirements to maintain a high radiation intensity for the third (and higher) harmonics of the spontaneous radiation. However, extra difficulties are posed by the small gap (6.35 mm in comparison with undulator A, which has a minimum gap of 10.5 mm); the strong vertical magnetic field (~ 1.33 Tesla), which makes it very difficult to accurately measure the horizontal magnetic field due to the planar Hall probe effect; and the long length of the device, c.f., undulator A is only 2.4 m long, whereas the prototype is 3.4 m long. The existing magnetic measurement facility at the APS is, however, well equipped and well suited to tune and measure the prototype undulator, and it has adequate resolution and reproducibility. The facility, the probes used, and the measurements of the assembled prototype are presented in this section.

4.2 Magnetic Measurement Facility

The APS magnetic measurement facility is equipped with a 6-m-long granite bench for Hall probe and moving coil measurements and a rotating coil system for first and second field integral measurements (see section 8.3.2 of the CDR for more details). (The rotating coil system was not used for the prototype undulator.) The key facility issues applicable to the prototype undulator are addressed in this section.

4.2.1 Hall Probes

For horizontal field measurements, two different Hall probes (Bell and Sentron) were tested, and it was found that the Sentron probes could be made to match the reference measurements made by the moving coil system after careful alignment of the probes and the undulator in the vertical direction.

4.2.1.1 Temperature Dependence

It is imperative that the magnetic measurements of the weak magnetic field dependence on temperature for the prototype undulator take into account the temperature dependence of the Hall probes themselves. Two recent Sentron Hall probes used at the APS showed a weak temperature dependence $\frac{(\Delta B / B)}{\Delta T} < 10^{-4} / ^\circ\text{C}$ in good agreement with the vendor's calibration. However, a third Sentron probe used for the prototype undulator showed much stronger temperature dependence with a large deviation from the

vendor's calibration. It was therefore accurately calibrated using the APS calibration magnet system. Fig. 23 shows the calibration results (deviation from linear dependency on the true field as measured by the nuclear magnetic resonance–NMR–probe) at the two temperatures used.

A single correction factor (1.0021) applied to the measured Hall probe voltages at 26.85°C makes the data coincide almost perfectly with the results obtained at 23.2°C (overlapping curves in the figure). Thus, a single correction factor is a very good approximation at all field strengths, and we derived the temperature dependence $\frac{(\Delta B / B)}{\Delta T} = +5.8 \times 10^{-4} / ^\circ\text{C}$ for this Sentron probe. A positive sign means that the Hall probe reads a larger voltage (magnetic field) with increased temperature. (This is opposite to the magnetic field dependence on temperature for the undulator.)

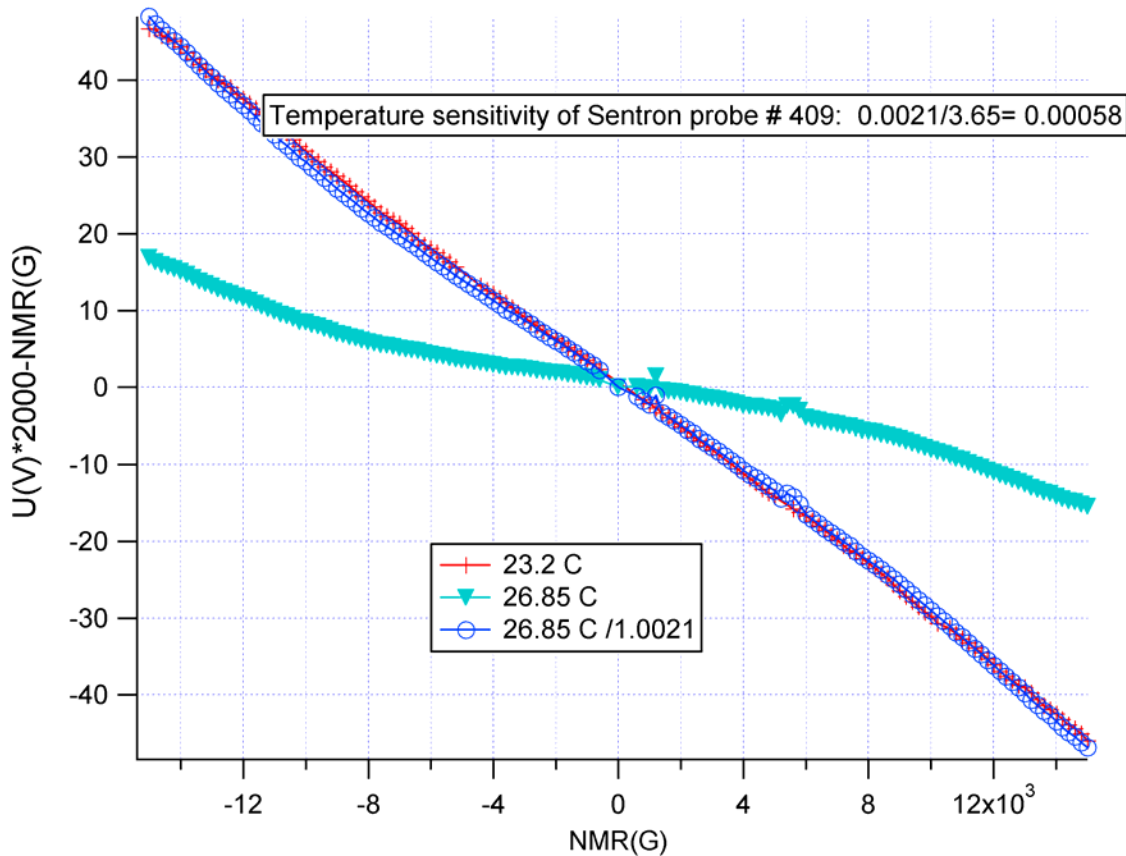


Fig. 23. Calibration of the Sentron Hall probe used for measurements of the prototype undulator. Calibration was done at the APS using the calibration magnet system with the NMR probe reading the reference field. The deviation from linear behavior is plotted for each curve. Two temperatures were recorded: 23.2°C (red crosses) and 26.85°C (cyan triangles). The data obtained at 26.85°C were divided by the correction factor 1.0021. The resulting data (blue circles) overlap with the curve at 23.2°C. The Hall probe temperature dependence of $(\Delta B / B)$ is $+5.8 \times 10^{-4} / ^\circ\text{C}$.

4.2.1.2 Horizontal Magnetic Field Measurement

In general, accurately measuring the horizontal magnetic field in the presence of the strong vertical field is difficult. The following precautions were taken to ensure that accurate measurements were obtained.¹⁵

- Test of Hall probe horizontal field measurements using the Sentron Hall probe and the APS undulator A in 1998 showed good agreement with moving coil reference measurements, demonstrating that the planar Hall probe effect and cross talk between the two sensors of the two-axis Sentron probe is small.
- The LCLS undulator is longer by 1 m and has a stronger vertical magnetic field that exaggerates the errors of the measurements. A test was performed to check the horizontal field readings of a Sentron probe in the presence of the vertical magnetic field.
- The results showed that, for small perturbations and a small horizontal magnetic field, this probe could be used for tuning, but final trajectory measurements should be compared with reference measurements taken using a moving coil.

4.2.2 Measurement Accuracy

The measurement accuracy and reproducibility of important parameters are listed in Table 6.

Table 6. Magnetic measurement accuracy and reproducibility.

Parameter	Value
Absolute Hall probe calibration accuracy	0.5 Gauss
Beam entrance/exit angle reproducibility	2.5 Gauss-cm (0.05 μ rad) *
Beam displacement at entrance/exit reproducibility	3400 Gauss-cm ² (0.7 μ m) *
rms B_{eff} error	0.15 Gauss
rms phase error	0.02°

* The angle and displacement are calculated for 14.35 GeV.

4.3 Measurements of the Assembled Prototype

4.3.1 Pole Gap

All sorting of magnet blocks and poles was done without precise prior knowledge of the actual pole-gap variations of the assembled magnetic structure. In fact, we worked under the assumption that the pole-gap variations might be as small as a few micrometers, which would then eliminate the need for magnetic tuning. (The rms pole-gap deviation of the sorted and paired poles before they were installed in the magnetic structure was only $2.4\ \mu\text{m}$, c.f., Fig. 20). However, pole-gap measurements of the assembled device showed deviations of up to about $\pm 50\ \mu\text{m}$ (Fig. 24), and tuning was therefore necessary. The relative large pole-gap deviations were found to be due to a combination of errors, arising from the aluminum base plates (flatness tolerance $50\ \mu\text{m}$), their attachments to the titanium housing and the machined precision of the housing ($50\ \mu\text{m}$).

Fig. 24 shows also the measured absolute value of the peak magnetic fields along the device (the first and last 5 poles are excluded). One should keep in mind that the field at any given pole is determined by several (~ 10) neighboring poles and a near-perfect linear correlation between the magnetic field and the gap is not to be expected. We observe a clear trend however, i.e., when the gap is large the magnetic field is small, and when the gap is small the magnetic field is large (see Fig. 24, near poles 80 and 110, respectively).

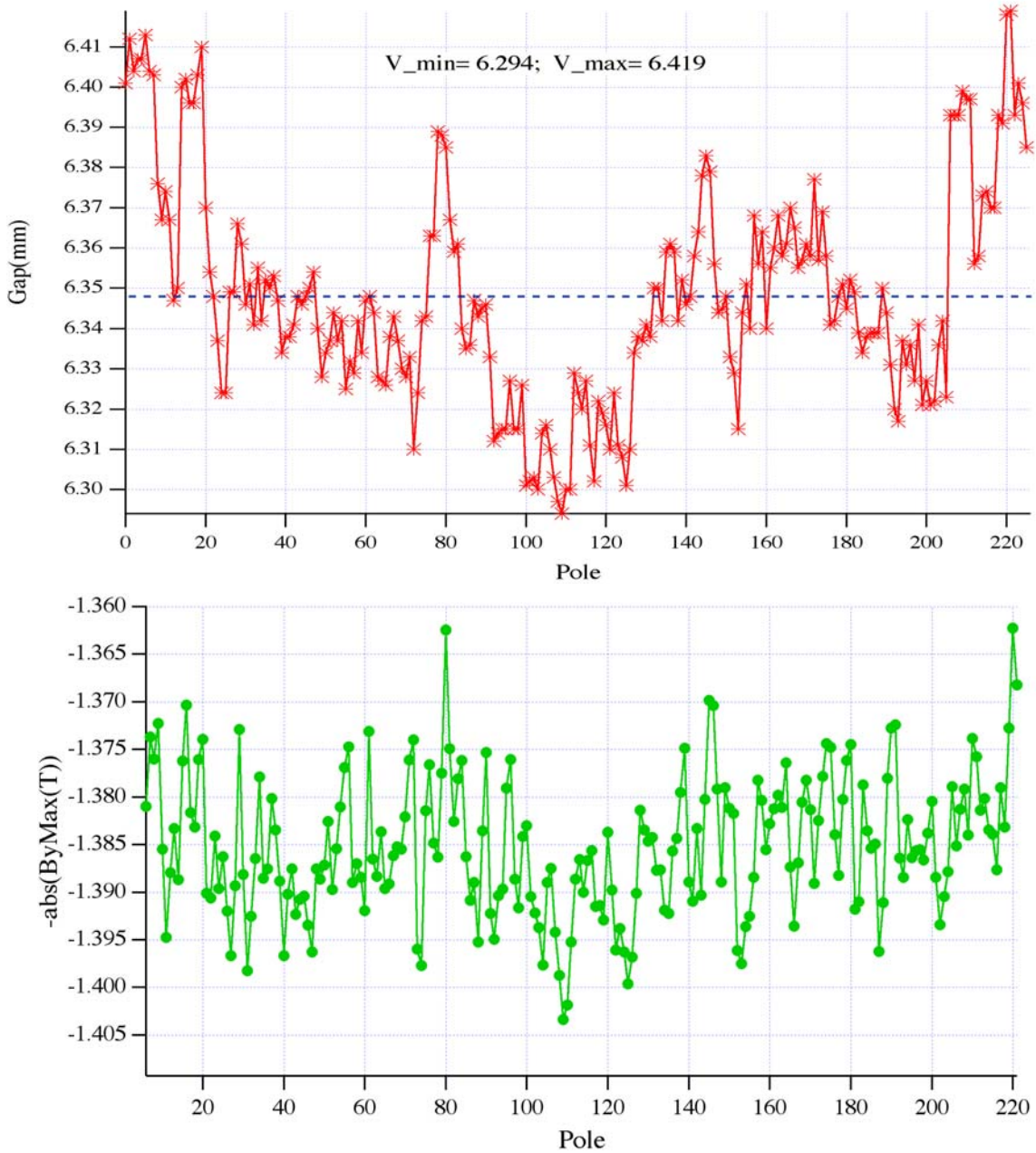


Fig. 24. Measured pole gaps (top) at all 226 poles and absolute value of the magnetic fields (bottom) at 216 poles (excluding 5 poles at the beginning and the end) along the length of the prototype after assembly. The average gap of 6.35 mm is indicated by the dashed line (top). Rather large pole-gap variations of $\sim \pm 50 \mu\text{m}$ can be seen. These deviations are much larger than the rms pole-gap variation of the sorted and paired poles ($2.4 \mu\text{m}$), see Fig. 20. The gap measurements are accurate to $\pm 1 \mu\text{m}$. The relatively large deviations are due to i) the aluminum base plates, which were machined to a flatness of $50 \mu\text{m}$, and especially ii) their attachments to the titanium housing. The large deviations near poles 15, 80, 145, and 210, all occur near the ends of the three $\sim 1\text{-m}$ -long base plates. The pole gaps for the two short end sections were about $50 \mu\text{m}$ larger than average.

4.3.2 Trajectory and rms Phase Error

The tolerance criterion for the trajectory deviations ($\pm 2 \mu\text{m}$ for both transverse planes) was met without tuning despite the rather large pole-gap variations; however, the calculated amplitude of the spontaneous emission was 7% smaller than ideal. Thus to improve the radiation amplitude, thin iron shims were applied to the surfaces of the magnets (so-called phase shims). To reduce the trajectory offsets and kicks, tuning was done by novel pole side shims for the vertical trajectory, and horizontal trajectory shims for the horizontal trajectory (shims are described in section 3.3.10). In total, 10 vertical trajectory shims, 16 horizontal trajectory shims, and 8 phase shims were applied to improve the performance.

Fig. 25 and Fig. 26 show the electron trajectories calculated from the Hall probe measurements before and after final tuning of the device. Similarly, Fig. 27 shows the calculated phase errors, also derived from Hall probe measurements, before and after tuning. The measurements were done at a gap setting of 6.35 mm (effective K value of 3.729). For the production undulators, a final gap adjustment will be made to set the K value equal to the design value of 3.710 (see discussions in section 6.3).

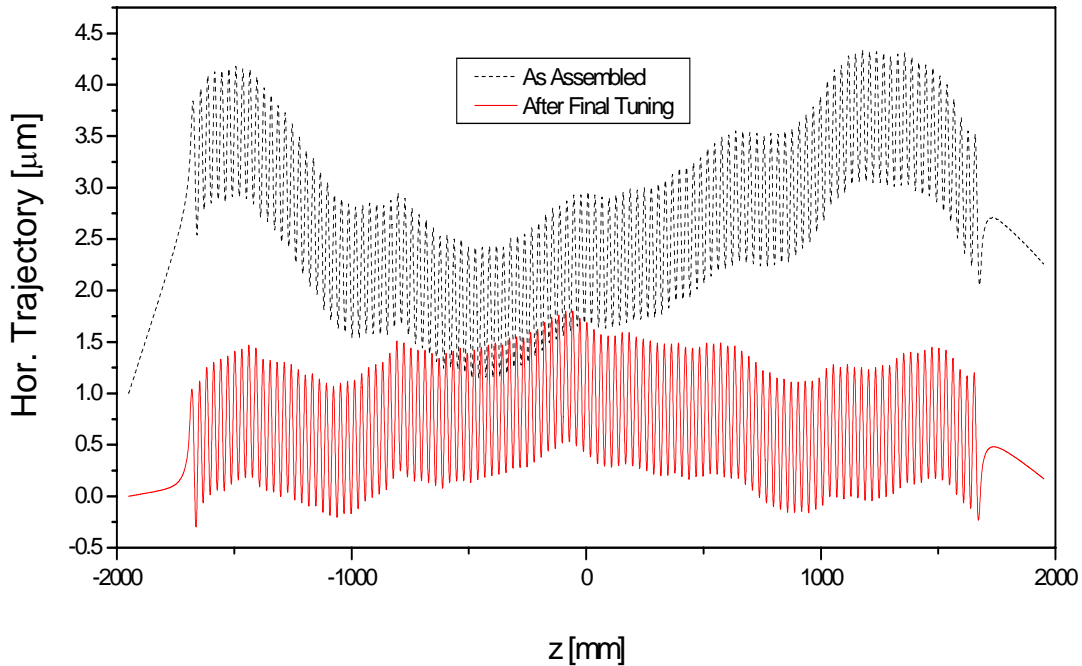


Fig. 25. Horizontal trajectory (from the vertical magnetic field) for the prototype as assembled (top black curve, displaced by $+1 \mu\text{m}$ to enhance clarity) and after final tuning (bottom red curve), calculated from Hall probe measurements at a beam energy of 14.35 GeV.

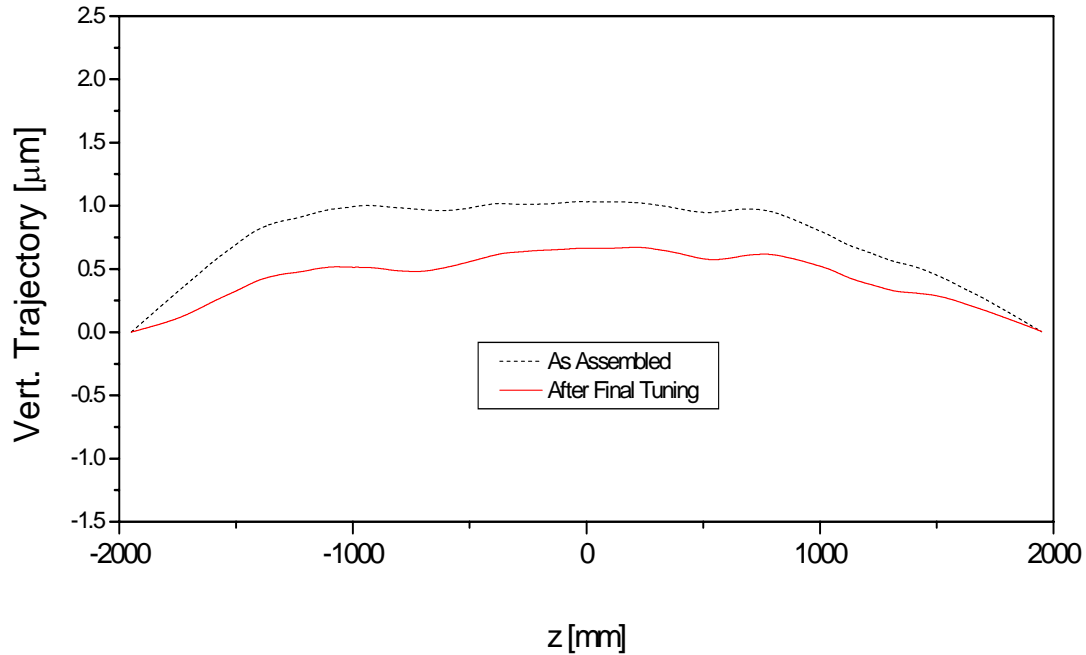


Fig. 26. Vertical trajectory (from the horizontal magnetic field) for the prototype as assembled (top black curve) and after final tuning (bottom red curve), calculated from Hall probe measurements at a beam energy of 14.35 GeV.

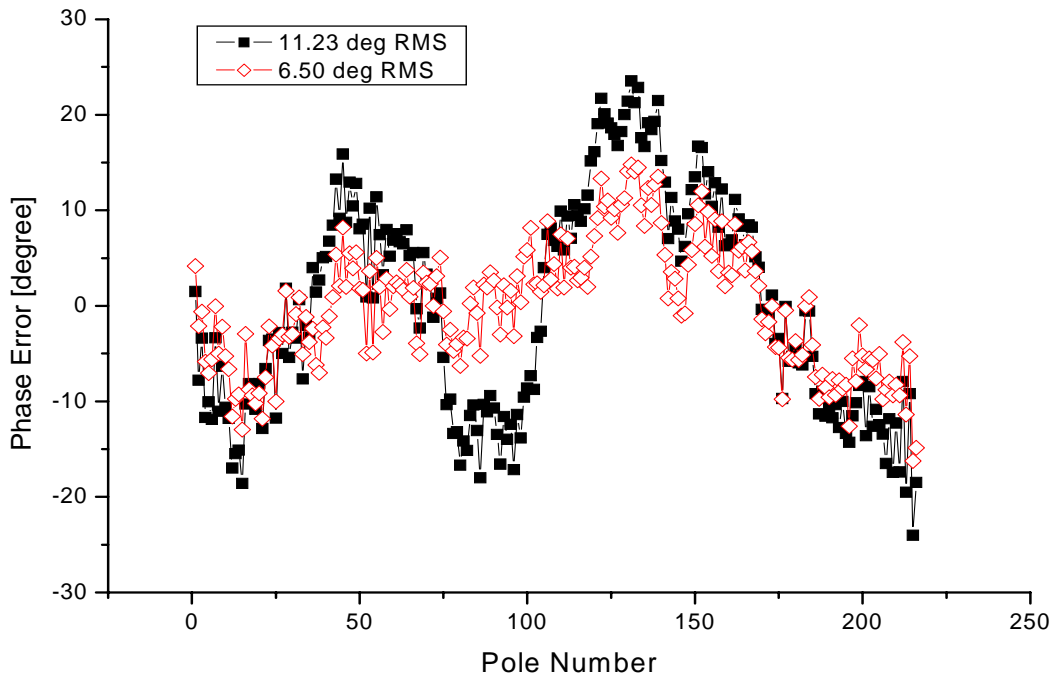


Fig. 27. Phase errors calculated from Hall probe measurements for the prototype as assembled (black filled squares) and after final tuning (red open diamonds). The rms phase error was reduced from 11.2° to 6.50° . The calculated amplitude of the spontaneous radiation is better than 99% of ideal after final tuning.

4.3.3 Temperature Dependence

Careful measurements of the effective magnetic field of the prototype undulator were made at two temperatures. In each case, the temperature was allowed to equilibrate for 48 hours. The prototype undulator temperature dependence, before being corrected for the Hall probe temperature dependence, was found to be

$$\frac{(\Delta B_{eff} / B_{eff})}{\Delta T} = +0.3 \times 10^{-4} / ^\circ\text{C}.$$

The Hall probe temperature dependence may be significant, as was discussed in section 4.2.1.1 for the Sentron probe used in this work. Thus, by subtracting the Hall probe temperature-dependent correction, we get

$$\frac{(\Delta B_{eff} / B_{eff})}{\Delta T} = -5.5 \times 10^{-4} / ^\circ\text{C}.$$

The previously reported measured temperature dependence ($-3.5 \times 10^{-4} / ^\circ\text{C}$) was a preliminary result for a partial assembly only. It should not be used.

The temperature sensitivity of the magnetic field has been partially compensated by the design, which automatically closes the pole gap with increased temperature. This compensating scheme relies on the large difference in thermal expansion between the aluminum base plates, the titanium housing, and the vanadium permendur poles, and has been estimated to contribute $\sim 0.010\%$ per $^\circ\text{C}$ (gap closes $\sim 0.7 \mu\text{m}$ per $^\circ\text{C}$). Thus, if the undulator gap were fixed, one would expect a value of $\sim 0.065\%$ per $^\circ\text{C}$, which is in reasonably good agreement with the estimate of 0.054% per $^\circ\text{C}$ (at fixed gap) reported in section 8.6.4 of the CDR.

It is worth mentioning that these measurements require extreme care and consideration of the different effects that may affect the final result of the measurements. For example, the large thermal mass of the undulator housing requires at least 24 hours to achieve equilibrium temperature. Fig. 28 shows the temperature relaxation time of the undulator housing (measured at both ends) compared to the fast relaxation time of the surrounding air.

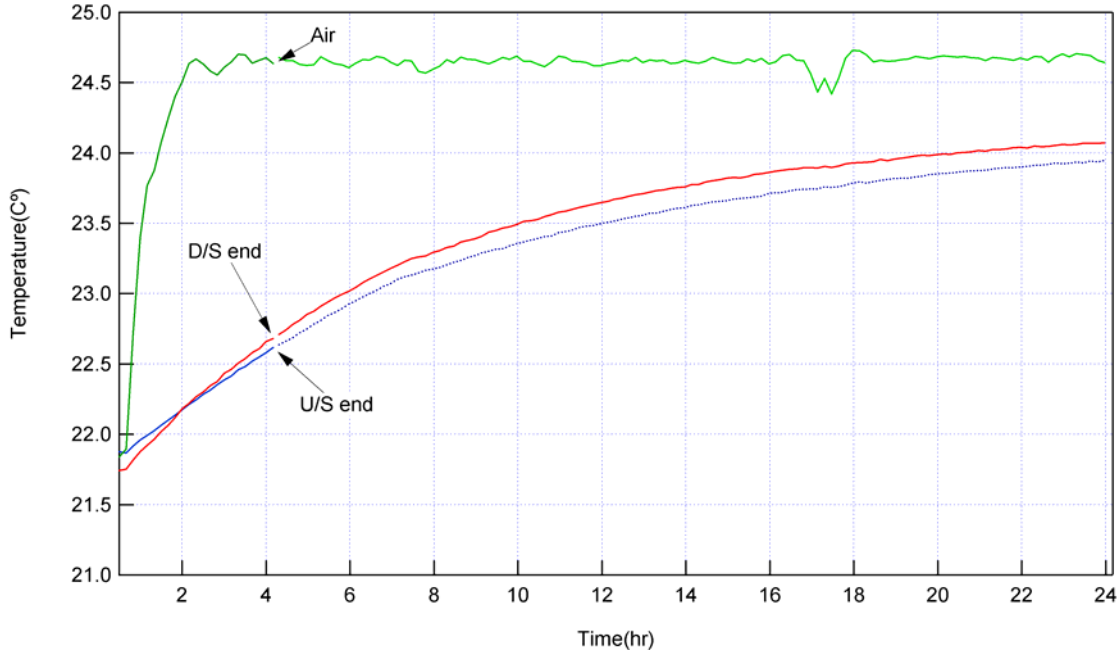


Fig. 28. Temperature relaxation time of the air temperature (top green curve) and the downstream (D/S; middle red curve) and upstream (U/S; bottom blue curve) ends of the undulator housing measured in the magnetic measurement facility at the APS. The air temperature was measured about 1 m away from the housing near the floor.

It is not even clear that all the parts of the undulator have reached their equilibrium temperatures after 24 hours, and different parts may be at different temperatures, which can produce localized distortions and affect the results. Thus an even longer settling time may be necessary to obtain the most accurate results.

4.3.4 Gap Dependence

A model calculation was performed using the code RADIA^{16,17} to estimate the gap dependence of the magnetic fields over large gap variations (both the effective field and the peak field). A comparison with the measured fields at 6.35 mm gap is also being made. The real geometry with period length 30.0 mm was used in the calculation. Permanent magnets made of NdFeB with a remanence magnetic field (B_r) of 1.24 T and vanadium permendur poles were assumed in the calculations (cf., the measured average $B_r = 1.246$ T for 500 magnet blocks, Fig. 17 in section 3.4.1.1).

The effective magnetic field and the peak magnetic field were calculated at 8 data points from 6.0 mm to 8.4 mm. Subsequently, a simple exponential, of the form $B(T) = B_0(T) * e^{(-q*gap)}$, where B_0 and q are unknowns, was fitted to the two curves. The fit deviated less than 0.4% (effective field) and 0.6% (peak field) at the data points, which is well within the margin of accuracy we are seeking here.

Table 7 lists the fitted parameters for the two fields. Fig. 29 shows the fitted gap dependence of the magnetic fields, and Fig. 30 shows the effective K value derived from the effective magnetic field. The absolute accuracy of the fields should not be assumed to be better than $\pm 1.5\%$ ($\pm 100 \mu\text{m}$ in gap).

Table 7. Fitted parameters for the effective and peak magnetic fields derived from model calculation using the code RADIA.

Parameter	Value
B_{eff0}	3.473 Tesla
q_{eff}	0.1506 mm^{-1}
B_{peak0}	3.811 Tesla
q_{peak}	0.1591 mm^{-1}

* The fitted gap dependence of $\Delta B_{eff}/B_{eff}$ of $1.5 \times 10^{-4}/\mu\text{m}$ differs slightly from the previously reported measured value ($1.4 \times 10^{-4}/\mu\text{m}$) obtained from measurements at two gaps (6.35 mm and 6.00 mm).

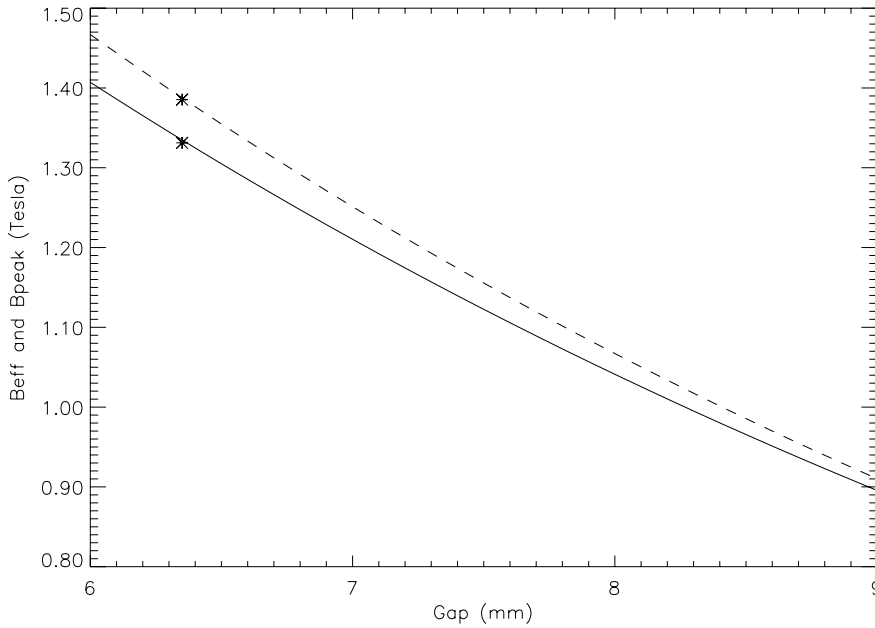


Fig. 29. Exponential fit to model calculations from code RADIA. The solid line shows the fitted gap dependence of the effective magnetic field (B_{eff}), and the dashed line the fitted gap dependence of the peak magnetic field (B_{peak}). The two stars at 6.35 mm gap are the measured values of the prototype undulator (no particular attempts were made to fine tune the model to match the measured data at those two points). The measured data points are 1.3312 and 1.3854 Tesla for the effective field and peak field, respectively.

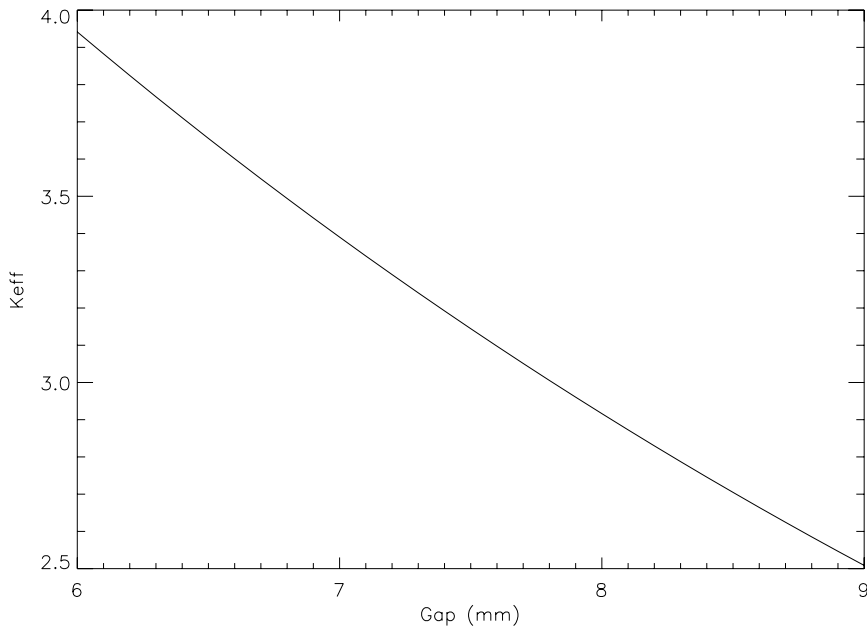


Fig. 30. The calculated gap dependence of the effective K value (derived from B_{eff} in Fig. 29). The measured effective field at 6.35 mm gap (1.3312 Tesla) corresponds to an effective K value of 3.729.

The previously reported measured gap dependence ($1.4 \times 10^{-4} / \mu\text{m}$) was derived from two gap measurements at 6.35 mm and 6.00 mm and differs slightly from the fitted value shown in Table 7. The measured fields at 6.00 mm gap were not obtained under such care as the results at 6.35 mm gap and were therefore omitted from the graph. (The measured effective field of 1.3954 Tesla at 6.00 mm gap would fall below the calculated value in Fig. 29.) For practical estimates near 6.35 mm gap, the value of $1.4 \times 10^{-4} / \mu\text{m}$ (1.9 Gauss/ μm) may be used.

4.3.5 Mechanical Stability

A test was performed to check the mechanical stability of the prototype undulator. The device was removed from the 6-m-long magnetic measurement bench and moved two turns around the APS storage ring on a fork lift (indoors). After the move, it was re-aligned at the bench, and the magnetic measurements were repeated. The results of the Hall probe magnetic measurements at 6.35 mm gap are shown in Table 8.

Table 8. Hall probe magnetic measurements of the prototype undulator at 6.35 mm gap before and after being moved two turns around the APS storage ring.

Case	B_{eff} (Gauss)	rms of B_{eff} (Gauss)
Before move (23.5°C)	13324.7	0.1
After move (23.6°C)	13324.3	0.22

We note that the difference between the two sets of measurements (0.4 Gauss) is much smaller than the tolerance requirement of ~ 2 Gauss, but it is bigger than the measurement error of 0.15 Gauss. However, it does not necessarily mean that the device changed during the transport. There are other effects, such as the alignment of the device to the bench, that affect the results. For example the same difference could be obtained if the device was shifted vertically by $40 \mu\text{m}$. Also, the same difference could be obtained if the device is off from the horizontal level by 0.1 degree due to the dependence of the Hall probe vertical field calibration on angle around the horizontal axis. The new support system, which will be used in the final stage of tuning of the production undulators, will allow even better alignment and better reproducibility.

The rms phase error of the device after the move was 6.58° , in agreement with the value of 6.50° obtained over one year ago (see Fig. 27 in section 4.3.2).

4.3.6 End-Phase Tuning

Remotely controlled piezoelectric translators were included in the design to vary the gap of the last seven periods at each end of the prototype undulator (see section 3.3.9). The phase adjustment has little effect on the spontaneous radiation from a single undulator segment (calculated to be less than 2% for the full range of gap change); instead it is intended to be used to adjust the phasing between the undulators to compensate for non-perfect matching of the effective magnetic field (effective K value) from one undulator segment to the next. It is anticipated that the adjusters will be used with the beam present to tune for maximum gain. However, new schemes have recently emerged for fine adjustment of B_{eff} , which may eliminate the adjustable end-gaps for the production undulator (see section 6.2).

A test was performed to measure the dependency of the phase slippage $\varphi(L)$ on the end-gap change (L is the total length of the undulator segment). The phase slippage derived from magnetic measurements is

$$\varphi(z) = k / 2\gamma^2 * [z + \int_0^z I_{1x}^2(z') dz' + \int_0^z I_{1y}^2(z') dz'],$$

where k is the radiation wave vector, γ is the relativistic factor, and $I_{1x,y}$ are the measured first field integrals of the transverse components of the magnetic field.

The derived slippage length, corresponding to 113 periods of phase slippage, was 3.668 m at 6.35 mm gap (effective K value of 3.729), which is somewhat bigger than design value of 3.607 m (see Table 2, footnote). This is partially due to the changed location of the magnetic shields at the ends of the device, see section 3.3.11. The actual slippage length is not important however, as long as the phasing condition is being met—actual setting of the break length between undulator segments needs to be determined by

magnetic field measurements with possible minor corrections applied determined by computer simulations. Fig. 31 shows the calculated phase slippage derived from magnetic measurement at five settings of the end-gaps. It shows that $\pm 100 \mu\text{m}$ change of the end-gap produces a $\pm 29^\circ$ (0.16 period) change of phase.

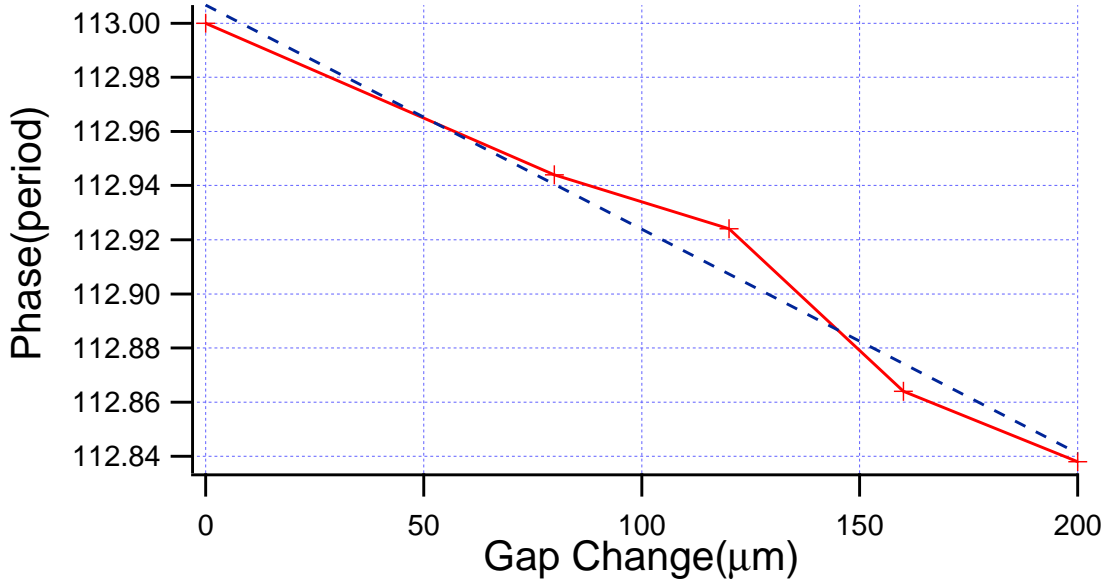


Fig. 31. Calculated phase derived from magnetic field measurements versus end-gap change (at one end of the undulator). The red crosses (connected by straight solid lines) are the measured data points, and the dashed blue line is a linear fit to the measurements.

Adjusting the phase between undulator segments can help correct for slightly different B_{eff} in the segments. The effect of this adjustment on the FEL performance can be studied by i) calculation of the complex amplitude of radiation, and ii) simulation of beam bunching (see section 2.2.1). In this section we report on the method of using the complex amplitude of radiation derived from magnetic measurements. The definition of the complex amplitude of radiation is (see section 8.2.4 of the CDR):

$$A(z) = \int_0^z I_{1y}(z') e^{-i\varphi(z')} dz',$$

where I_{1y} is the measured vertical first field integral of the magnetic field; the phase slippage φ was defined above. The absolute value of the complex amplitude of radiation $|A(L)|$ (length of the vector) defines the intensity of the spontaneous radiation.

First the complex amplitude of radiation was compared to an ideal case, where the regular part of the device was represented by a perfect vertical cosine-like longitudinal field distribution and the ends were taken from the measured data. The $|A(L)|$ derived

from measurements was found to be almost 100% of ideal. The radiation wavelength used in the calculations was 1.5 \AA , and the particle beam energy was 14.35 GeV .

The case for two undulator segments in a row was examined next. The measured magnetic field of the prototype undulator was used for the second device, and a change of the field was artificially implemented for the second device to check the sensitivity to field perturbations. This was done by multiplying the magnetic field by an appropriate factor. (In reality, such a change would correspond to a change of either the pole gap or the temperature.) Fig. 32 shows the case for two undulator segments in a row when the magnetic field of the second device has a smaller effective magnetic field ($\Delta B_{eff}/B_{eff} = 7.0 \times 10^{-4}$) and no phase correction was used. (The field change of 7.0×10^{-4} was chosen because it was estimated to correspond to a 2°C temperature rise derived from early measurements of the undulator magnetic field temperature dependence, see section 4.3.3).

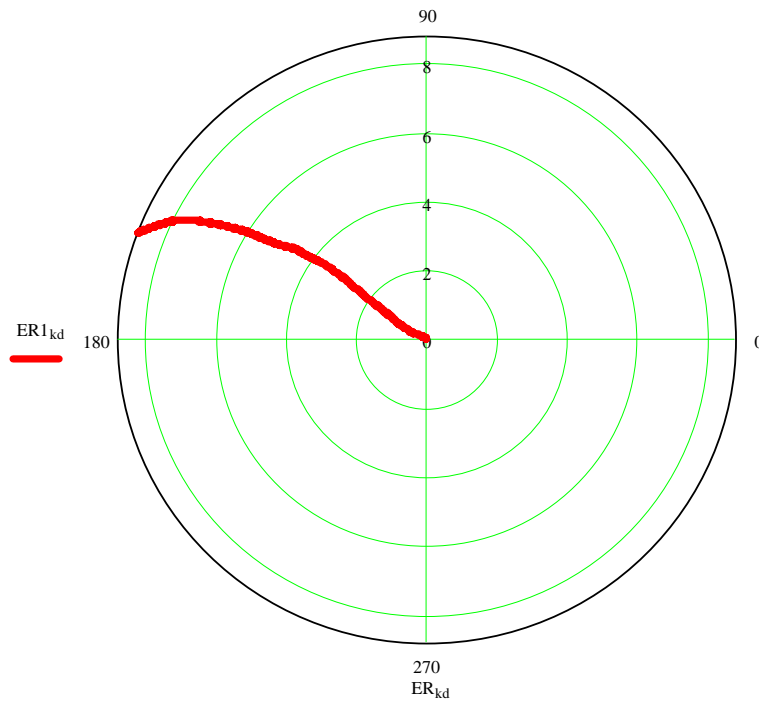


Fig. 32. Polar plot of $|A(z)|$ versus $\arg(A(z))$ at 1.5 \AA and 14.35 GeV with no end-gap adjustments between two undulator segments. The magnetic field of the second device was made smaller by 0.07% (corresponds to $\sim 5 \text{ \mu m}$ gap change). Because of the mismatched phase between the two devices, the near straight behavior of $|A(z)|$ starts to curve, and the magnitude becomes smaller than ideal.

There is a degradation of $|A(L)|$ by about 5% compared to ideal. To compensate for this deviation, the phase between the two devices was tuned to achieve the highest

possible amplitude of radiation. A change of phase of 0.068 (24.5°) was found to be optimum, and the result is shown in Fig. 33. The $|A(L)|$ is now 98.4% of ideal, and the degradation is less than 2% as required.

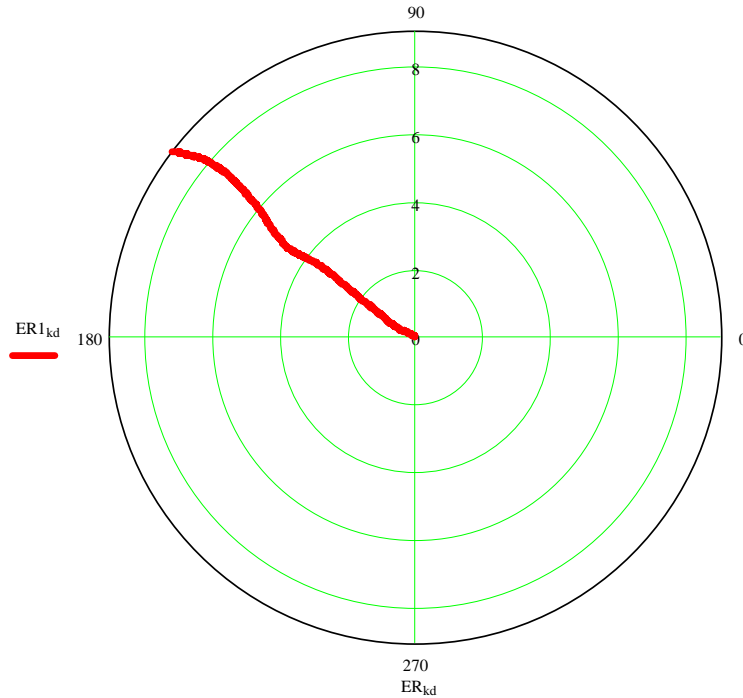


Fig. 33. Phase correction of 24.5° implemented with respect to the case shown in Fig. 32.

Only a portion of the full range of end-phase corrections was used here (24.5° out of 29°), which means that the built-in range ($\pm 100 \mu\text{m}$) of the end-gaps is more than sufficient for compensating $\Delta B_{eff}/B_{eff}$ up to 7.0×10^{-4} . Larger field deviations may not be acceptable, because the correction of such distortions, although helpful, may not be sufficient to satisfy the requirement to limit the degradation of the radiation amplitude to less than 2%. The end-phase tuning could also be used to correct slight longitudinal placement errors of the devices. The existing phase tuning allows one to correct drift space misalignments of up to 7.6 cm, which is far beyond any practical need. The results obtained here agree with the results of computer simulations of the FEL gain to study end-phase compensation (see section 2.2.1), when beam emittance, beam energy spread, etc., are taken into account.

5 Summary

A full-length prototype undulator segment was successfully built, magnetically tuned and characterized. The prototype proved to meet all stringent mechanical and magnetic tolerances after a few design changes were made and final magnetic tuning was completed. A summary of the important lessons learned from our experience with the prototype is given below. The issue of setting the effective magnetic field B_{eff} to a tolerance of $\sim 1.5 \times 10^{-4}$ for all undulator segments is still under investigation and is discussed in detail in section 6.3.

5.1 Magnetic Design

- The magnetic design proved to provide higher than required magnetic field at the nominal gap of 6.00 mm. An effective K value of 3.729 was measured at a gap of 6.35 mm. (The design K value of 3.710 is obtained at ~ 6.4 mm gap.)
- After extensive discussions regarding using SmCo magnets for the design, a choice was made to stay with NdFeB magnets for the production undulator.

5.2 Mechanical Design

- One clamp per pole was not sufficient. The design was changed to include two clamps per pole.
- The measured pole gap variations ($\pm 50 \mu\text{m}$) over the length of the device were larger than expected (due to primarily the aluminum base plates and their attachments to the housing).
- The window of the titanium housing was manufactured with a precision of $50 \mu\text{m}$ over its entire length.
- The remotely adjustable end-gaps were found to work as expected and to provide sufficient tuning range to compensate for B_{eff} variations up to $\sim 7.0 \times 10^{-4}$. (Their long-term stability and reliability is yet to be tested.)
- The measured temperature dependence of the undulator effective magnetic field was in reasonably good agreement with magnetic design calculations.
- The rigid design was tested, and magnetic measurements were done. No stability issues were found.
- Mechanical shims with incremental thickness with a tolerance of $\sim \pm 2.5 \mu\text{m}$ can be fabricated (used for tuning the effective magnetic field).

5.3 Tuning and Measurements

- Larger than desired pole-to-pole variations in the magnetic field of the assembled device were measured.
- The variations in the magnetic moment of the magnet blocks after sorting or in the pole heights of the individual poles after sorting were not dominating factors contributing to the relatively large pole-to-pole magnetic field variations. The variations in the magnetic field were found to correlate with pole-gap variations.
- Measuring each individual magnet block's magnetic moment for the production undulator will not be necessary. Simple sorting by pairing weak and strong magnets based on the vendor's data is sufficient.
- The pole heights will be measured and paired for the production undulator. Although not critical, it will improve the pole-gap variations.
- The prototype was tuned in two days to achieve better than the required tolerances. The high quality of the magnets and the high mechanical precision and rigid design made this possible.
 - Tolerance for trajectory walk-off: 2 μm (required), 0.5 μm (achieved, both planes).
 - Tolerance for radiation amplitude deviation: 2% (required), < 1% (achieved).
- The APS magnetic measurement facility provides the necessary accuracy and reproducibility of important parameters:
 - Absolute Hall probe calibration accuracy, 0.5 Gauss
 - Beam entrance/exit angle reproducibility, 2.5 Gauss-cm (0.05 μrad)
 - Beam displacement at entrance/exit reproducibility, 3400 Gauss-cm² (0.7 μm)
 - rms B_{eff} error, 0.15 Gauss
 - rms phase error, 0.02°
- The time required for tuning the effective magnetic field to a specific value to the required accuracy of $\sim 1.5 \times 10^{-4}$ can be determined once the tuning method has been decided.

shunt), and ii) the end phasing may not be necessary when using a canted pole-gap design (see section 6.3.3 for the canted pole-gap design).

5.4.4 Cam-Shaft Movers

The cam-shaft movers will be rotated 180° in the horizontal plane to keep motors (and encoders) shielded from radiation by the gearboxes. The self-aligning double-row spherical ball bearings will be replaced by double-row ball bearings. This will reduce the alignment error to about 5 μm and 10 μm in the vertical and horizontal directions, respectively.

5.4.5 New Support Pillars

New support columns will allow for manual mechanical alignment of the undulator segments.

6 Other Studies

6.1 SmCo versus NdFeB

Studies on the selection of “best” magnet material for the LCLS production undulator have been done. Magnets of SmCo are, in general, more radiation resistant than NdFeB magnets. Their remanent field is lower however (~ 8% for the magnets under consideration), giving a smaller undulator B_{eff} for the same pole gap, and they are about two times less sensitive to losing remanent field with increased temperature. However, there may be assembly issues, because SmCo magnets are brittle and magnetic material may break off, and special care may be required in handling large quantities. They are also significantly more expensive. This section addresses these important issues in more detail.

6.1.1 Radiation Damage

6.1.1.1 Introduction

Potential radiation-induced demagnetization of the permanent magnets is a critical issue. The radiation damage of materials is, in general, a function of the type and energy of the radiation, the integrated dose and dose rate, the irradiation temperature, the sample geometry, the irradiation history, and the manufacturing process and impurities. The main issues with respect to radiation damage at the LCLS are:

- Relative radiation resistance of SmCo and NdFeB magnets in the radiation environment expected at the LCLS.
- Duration of baseline operation that the undulator system can withstand before it develops radiation damage.

- System optimization for minimum beam losses.

In order to investigate these issues, a literature survey was performed in addition to data collected from the APS experience^{6,7} with respect to the radiation sensitivity of permanent magnets. However, comparisons between published data on relative radiation resistance of permanent magnets are not always accurate, since there are factors, such as irradiation temperature and sample geometry (i.e., the effective demagnetizing field), that are not the same.

Irradiation of SmCo and NdFeB magnets has been performed under several radiation environments: neutrons, protons, heavy ions, bremsstrahlung, low-energy gamma rays, low- and medium-energy electron beams, and 2 GeV electron beams. However, most of the experiments that report relative radiation performance of SmCo and NdFeB magnets are quite old, and significant advances have occurred in permanent magnetic materials since then. Some of the main conclusions that have been reached to date (for irradiation environments other than 2 GeV electron beams) are:¹⁸

- SmCo magnets are, in general, more radiation resistant than NdFeB magnets regardless of the source of radiation (i.e., neutrons, photons or charged particles). The order of radiation resistance appears to be Sm₂Co₁₇, SmCo₅ and Nd₂Fe₁₄B.
- A trend has also been observed that the higher the coercivity the higher the radiation resistance.
- Significant differences in radiation resistance have also been observed between magnets from different vendors that appear to be due to microstructural differences, manufacturing processes and impurities.
- The superiority of SmCo with respect to radiation damage is believed to be due to its higher Curie temperature (e.g., 820°C or 780°C depending on grade). Adequate models for the mechanism of damage are not available for the various radiation environments.

Results from representative publications on relative radiation resistance of NdFeB and SmCo magnets under different radiation environments are presented in the following sections.

6.1.1.2 Neutron Irradiation

Irradiations performed by Cost et al.¹⁹ have shown that SmCo magnets had good radiation resistance even at 10¹⁸ n/cm², while NdFeB magnets showed significant degradation at 10¹⁵ n/cm² and 10¹⁶ n/cm². However, they also showed that a certain type of NdFeB had significantly higher resistance than the rest though still worse than the

SmCo samples. The irradiations were performed with fast neutrons ($E > 0.1$ MeV) at 350 K, in the Omega West nuclear reactor at the epithermal cadmium port.

In addition, due to the high cross section of boron for thermal neutrons, they studied possible damage due to thermal neutrons. No significant radiation damage of the NdFeB magnets was found, up to the fluences used in their experiments.

6.1.1.3 Proton and Heavy Ion Irradiation

High-energy (500 MeV) proton irradiations showed that SmCo magnets were sensitive only in the giga-gray range, while NdFeB magnets were already sensitive in the mega-gray range. Similar differences in radiation resistance were observed when irradiating with deuterons (106 MeV), for doses up to 30 kilo-gray.²⁰

6.1.1.4 Low- and Medium-Energy Electron Irradiation

Under irradiation with 17 MeV electrons at a dose equal to 2.1×10^{-3} C/cm², the flux loss for NdFeB magnets was 9%, while, for an electron dose equal to 1.4×10^{-3} C/cm², the SmCo showed a flux loss less than 0.4%.²¹ The electron dose received by the SmCo magnets was 2/3 of that received by the NdFeB magnets, but the flux loss was much smaller than that ratio. Experiments have also been performed with 180 MeV electron beams.²² In those experiments, the magnets were placed in a stack, and the demagnetization was a function of their position in the stack. The SmCo magnets did not show significant demagnetization at approximately 70 Mrad, while the NdFeB magnets showed partial demagnetization.

6.1.1.5 Low-Energy Gamma Ray Irradiation

Both NdFeB and SmCo magnets showed very good radiation resistance (i.e., flux loss below 0.5%) even at absorbed doses equal to 2.8 mega-gray when irradiated with a Co-60 source (i.e., 1.173 MeV and 1.332 MeV gamma rays).

6.1.1.6 Low-Energy Bremsstrahlung Irradiation

Bremsstrahlung irradiations using an 85 MeV electron beam²³ resulted in signs of demagnetization in NdFeB at an absorbed dose of 0.45×10^9 rad, while SmCo did not show any demagnetization even at approximately twice this dose (1.27×10^9 rad).

6.1.1.7 Electron Beam (2 GeV) Irradiation

To date the published data that are most relevant to the irradiation environment that is to be expected at the LCLS are those reported by Bizen et al. using 2 GeV electron beams at the Pohang accelerator.²⁴ These experiments suggest that the performance of high-coercivity NdFeB magnets at this radiation environment is comparable to that of the SmCo magnets. Experiments were performed using one SmCo magnet and several

NdFeB magnets with different coercivities. They found that some of the higher coercivity NdFeB magnets had worse radiation sensitivity than NdFeB magnets with lower coercivity, although for magnets from a single vendor, higher coercivity was correlated with higher radiation resistance. In addition they found that one of the NdFeB magnets that had the highest coercivity was more radiation resistant than the SmCo magnet.

6.1.1.8 Future Directions

The majority of the published data has shown that SmCo magnets are systematically more radiation resistant than NdFeB magnets under various radiation environments. In addition, the higher coercivity SmCo magnets proposed for the LCLS would probably exhibit higher radiation resistance than that observed in the 2 GeV experiments because their coercivity is higher.

The NdFeB magnets used for the insertion devices at the APS have also shown significant radiation-induced demagnetization. Many of these magnets were purchased from Shin-Etsu (grade N38H) and have a coercivity of ~ 1400 kA/m. Thus, the published data suggest that, based on relative radiation resistance considerations alone (especially for a mixed radiation environment), the SmCo material appears to be the preferred choice. However, due to the lower remanent magnetic field and the higher cost of SmCo magnets, high coercivity NdFeB magnets should also be explored further.^{25,26}

If the process producing the radiation-induced demagnetization is known (from controlled measurements or modeling), then the damage threshold and subsequently the time until significant radiation damage is observed can be estimated. Modeling efforts could also be extended to system optimization with respect to beam losses from misteered beam strikes and particle strikes from the beam halo. Such research has been initiated for the LCLS (see section 14.2.2 of the CDR).

6.1.1.9 Magnet Choice

Due to uncertainty in the dose required to achieve significant radiation damage, the damage mechanism, the precise geometry, etc., and based on our proven ability to construct the prototype undulator with NdFeB magnets, we have chosen to minimize our schedule risk and stay with NdFeB. Significant effort will instead be applied to preventing any significant dose of radiation to the undulators. Furthermore, we will construct six additional spare undulators to be used in a periodic exchange/maintenance schedule.

6.1.2 Magnetic Field Considerations

Two types of permanent magnets and corresponding remanent fields and coercivities that have been considered for the production undulator are shown in Table 10. The gap dependence of the effective magnetic fields was calculated for the LCLS undulator design using the code RADIA, and the result is shown in Fig. 34.

Table 10. Magnet materials and grades under consideration for the production undulator.*

Magnet material	Grade	Manufacturer	Remanence B_r (Tesla)	Coercivity H_{cj} (kA/m)
Sm_2Co_{17}	R32HS	Shin-Etsu	1.12 – 1.20	1591 – 2387
NdFeB	N39UH	Shin-Etsu	1.22 – 1.28	1989

* NdFeB (grade N39SH) magnets from Shin-Etsu with a vendor-specified remanence field of 1.23 – 1.29 Tesla, and coercivity of 1671 kA/m were used for the prototype undulator. As delivered, the average remanent field was 1.246 Tesla for a batch of 500 magnet blocks (see Fig. 17).

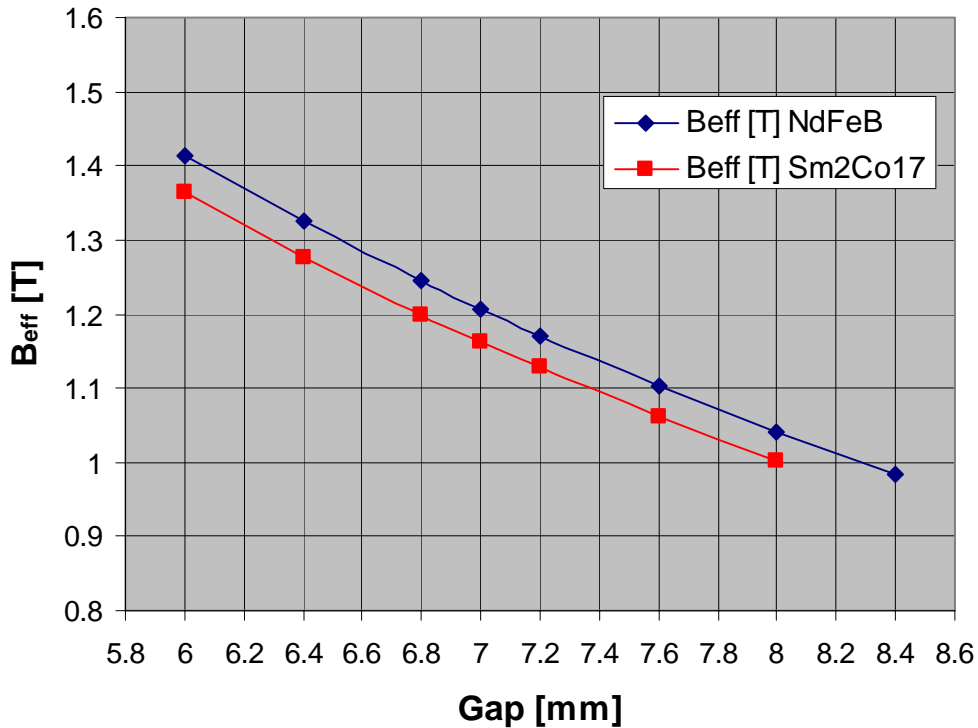


Fig. 34. Calculated gap dependence of the effective magnetic field for Sm_2Co_{17} ($B_r = 1.14$ Tesla) and NdFeB ($B_r = 1.24$ Tesla) magnets for the LCLS undulator design using the code RADIA.

There is a reduction of the effective magnetic field for a design using magnets made of $\text{Sm}_2\text{Co}_{17}$ due to their lower remanent field. The use of NdFeB saves approximately 0.2 mm gap for the same effective field as $\text{Sm}_2\text{Co}_{17}$.

6.1.3 Temperature Dependence

The remanent field B_r decreases by 0.05% per °C for NdFeB magnets, and decreases by 0.03% per °C for SmCo magnets, in the temperature range 20 – 40°C.²⁷

The measured decrease of the effective magnetic field B_{eff} at the undulator gap center was 0.055% per °C (for NdFeB). The gap closes with increased temperature, and it was estimated to contribute ~ 0.010% per °C (see section 4.3.3). However, due to uncertainties in the estimate of the gap closing and due to saturation effects in the poles, a direct comparison with the vendor's specified temperature dependence of B_r is not exact.

Thus, it is difficult to estimate the undulator B_{eff} temperature dependence for a design using SmCo magnets. A rough estimate can be done however, by using the temperature dependence of B_r as a guidance, in which case a temperature stability of ~ ±0.5°C would be required.

6.1.4 Other

The SmCo magnets are brittle and special care in handling large quantities may be needed. For example, small pieces may break off the blocks, and although the loss of magnetic material may not directly affect the magnetic properties, micron-sized pieces stuck between the aluminum base plate and the pole will change the pole gap, and hence the on-axis field strength. The cost for SmCo magnet blocks is higher than NdFeB by about a factor of two.

6.2 End Phasing

The need for built-in and remotely adjustable end phasing is currently being discussed. In fact, it may not be needed, although variations in B_{eff} up to $\sim 7.0 \times 10^{-4}$ between undulator segments can be compensated (see sections 2.2.1 and 4.3.6). (A variation in B_{eff} of 7.0×10^{-4} corresponds to a gap change of $\sim 5 \mu\text{m}$ or a temperature change of $\sim 1.3^\circ\text{C}$.) The temperature sensitivity of B_{eff} depends on the magnet material used for the undulator. The required tolerance of $\sim 1.5 \times 10^{-4}$ for B_{eff} corresponds to temperature stability of $\sim \pm 0.3^\circ\text{C}$ for the current undulator design, which uses NdFeB magnets (see section 6.1.3 for a comparison with SmCo magnets).

Two following two cases can be identified:

1. The B_{eff} will be tuned to an accuracy of $\sim 1.5 \times 10^{-4}$, and temperature-induced variations in B_{eff} , would be compensated by a change of phase at the ends (either by varying the end-gaps or by using a magnetic shunt applied to the ends, see section 6.3.2). Or it could be achieved using the latest idea of a canted pole-gap design (yet to be tested), where the undulator, as a whole, moves in the transverse direction and end phasing would not be necessary (see section 6.3.3).
2. The B_{eff} will be tuned to an accuracy of $\sim 7.0 \times 10^{-4}$, with end-phase compensation applied as in 1). Additional means to compensate for temperature variations must be provided in this case.

A correct B_{eff} is not sufficient to satisfy the 10° phase-slippage tolerance requirement, however. Therefore, end-phase *tuning* will always be needed to set the correct phase slippage. This can be done in several ways: 1) with variable end-gaps, as in the current prototype, or 2) with shunts at the ends, or 3) with a combination of regular phase shims and mechanical shims,²⁸ or 4) with adjusting of the longitudinal position of the magnetic shield. The variable end-gaps and the shunt, if implemented, may be remotely controlled, if necessary.

6.2.1 Remotely Adjustable End-Gaps

The long-term stability and reliability of the remotely adjustable end-gaps are yet to be tested.

6.3 Fine Adjustment of Effective Magnetic Field

The requirement to set and maintain the magnetic field very precisely along the entire undulator line ($\Delta B_{eff}/B_{eff} \sim 1.5 \times 10^{-4}$ from one undulator segment to another) is challenging. The measured gap dependence of $\Delta B_{eff}/B_{eff}$ of $\sim 1.4 \times 10^{-4} / \mu\text{m}$ shows that the gap needs to be set with one-micron-level precision, which is impossible to do (in this design). Instead, we will rely on mechanical shims to initially set the pole gap to a tolerance of about $\sim 10 \mu\text{m}$ (see section 6.3.4). Thereafter, the B_{eff} can be adjusted as discussed below to the required tolerance of $\sim 1.5 \times 10^{-4}$ (or $\sim 7.0 \times 10^{-4}$, if end-phase compensation is used).

Temperature regulation of each undulator segment with a stability of $\pm 0.3^\circ\text{C}$ was the first idea under discussion. A few different ways to regulate the temperature have been examined, but we found that all of them would be very complicated, costly, and, due to the large thermal mass, will require many hours for temperature stabilization.

Two other options were recently proposed to provide for such tuning. The first idea was to locate a low-carbon steel shunt inside the back of the base plates that hold the magnets and poles. The second idea was to use a canted pole-gap design and move the whole undulator segment transversely in the horizontal direction in and out of the beam.

This section summarizes the current issues involved for each of these ideas. All of this is work in progress.

6.3.1 Temperature Regulation

A temperature-control study was performed, and a summary of the main advantages and disadvantages for each case is given in this section.

6.3.1.1 Air Cooling/Heating

The advantages and disadvantages of using an air-temperature-controlled enclosure are listed below.

Advantages

- Does not impact the undulator design.
- Stabilizes the entire structure including diagnostics.
- Commercially available enclosures can be tailored to our applications.

Disadvantages

- Reduces easy access to undulators.
- More difficult to precisely control air temperature compared to water cooling.
- Achieving 0.3°C temperature stability is difficult (1°C is more standard).
- Fine control can only be achieved by pushing large volumes of air through the enclosures and may result in vibrations.

6.3.1.2 Water Cooling

The advantages and disadvantages of using water cooling are listed below.

Advantages

- Access to undulators not restricted.
- Relatively easy to implement cooling design.
- Cooling passages can be an integral part of the housing.
- Achieving 0.1°C temperature stability with water is relatively easy.

Disadvantages

- Poor conduction path between the housing and the aluminum base plates (that hold the magnets and poles). Modifications may be needed.
- Can not easily achieve uniformity along the undulator line (importance of temperature gradients needs to be studied).
- Though reduced, there will still be temperature fluctuations as a function of changes in room temperature.

6.3.1.3 Active Heating

The advantages and disadvantages of using active heating are listed below.

Advantages

- Can use commercially available heaters and control systems.
- Fine control is possible if the heater layout design is properly done.

Disadvantages

- Very complicated heater layout required to achieve stability and uniformity.
- Complicates the undulator design and fabrication.
- Sophisticated variable power and PID control system required for each undulator.
- Gradients are inherent in the design.

6.3.2 Shunt

The idea of using a low-carbon steel shunt located inside the back of the base plates was recently tested. An optimization of the shunt cross section, its location and travel range was done, and Fig. 35 shows the actual dimensions derived from calculations made by code RADIA. The model is shown in Fig. 36, and the estimated peak field variations are shown in Fig. 37, using NdFeB magnets with a remanent field of 1.24 Tesla. Results are shown versus position for both simultaneous motion of both shunts located inside the top and bottom halves of the magnet structure and for only one shunt moving.

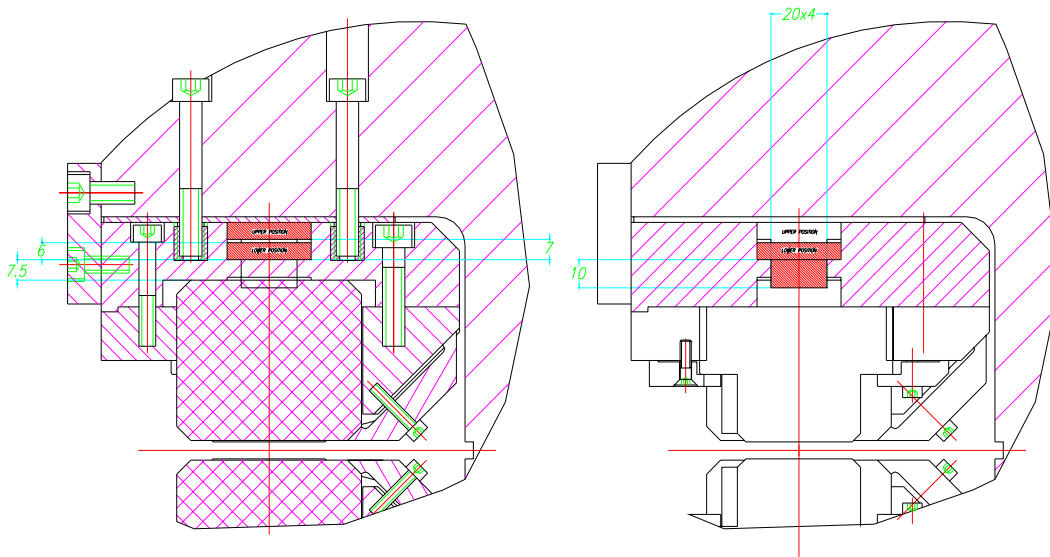


Fig. 35. Magnet shunt design and location. Left: cross section through the magnets and the backing iron. Right: cross section through the poles and the comb that are near the back of the poles.

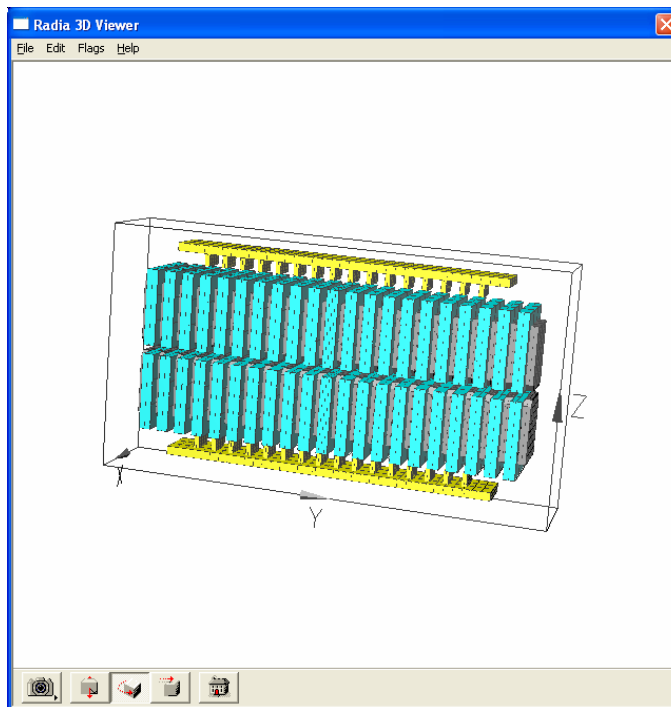


Fig. 36. Model used in RADIA for calculation of change of peak field versus location of the comb. The cross section of the backing iron is $36 \times 6 \text{ mm}^2$, and the comb dimensions are $4 \times 20 \times 10 \text{ mm}^3$.

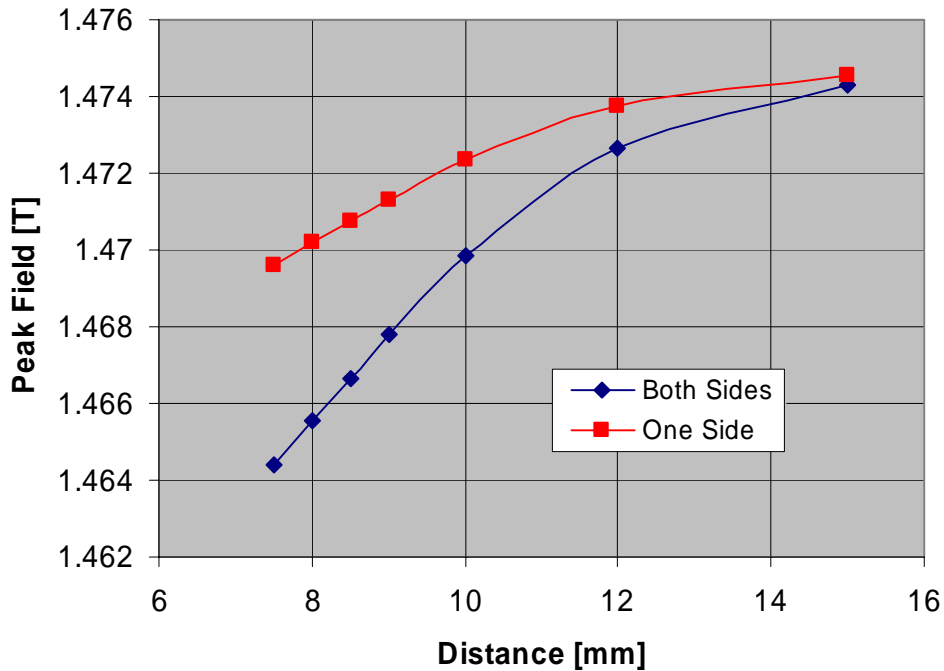


Fig. 37. Calculation of peak magnetic field versus position of comb from location nearest to the poles (7.5 mm) to fully extracted (15 mm) using code RADIA for NdFeB magnets with a remanent field of 1.24 Tesla. The top red curve is for using one shunt only. The bottom blue curve is for using two shunts, one for each jaw. The predicted change in peak field is 49 Gauss using one shunt over the full range of travel and about 100 Gauss using two shunts.

This idea relies on the fact that the field change does not depend sensitively on the position of the shunt. A positioning accuracy of 0.1 mm (2 Gauss) is sufficient and corresponds to a change of the magnetic field of $\sim 1.5 \times 10^{-4}$.

A test using the comb was performed. It was installed in one base plate in one of the three ~ 1 -m-long pieces (one jaw only). The pole gaps and magnetic fields were measured for: i) the comb near the poles, and ii) extracted by ~ 7 mm, and the measured magnetic field was corrected according to the measured pole gaps. The measured peak field difference was 27 Gauss. This is considerably less than the calculated 49 Gauss; however, the measured value is not particularly accurate. In this first test case, changing the comb position required disassembling and reassembling the magnet array section. This resulted in small pole-gap changes, and the measurements had to be corrected for these changes. However, even with this performance, the following scenario looks feasible. The first step would be to set the desired field with mechanical shims with thickness steps of 0.01 mm (a correction of less than 20 Gauss will then be required). The next step would be to adjust the comb for the upper jaw only to set the desired field value.

6.3.3 Canted Pole Gap

One of the options to set the magnetic field with an accuracy of $\sim 1.5 \times 10^{-4}$ for B_{eff} is to use a canted design, in which the pole gap is not constant but varies linearly with the horizontal direction. In the case of a small cant (a few milliradians), the magnetic field is approximately proportional to the pole gap over a small gap range and hence to the horizontal position. For the proposed canted pole-gap design, the poles alone are not canted. Instead the aluminum base plates will be machined with the appropriate cant.

Additional requirements that arise in this case are associated with providing stability of B_{eff} with the mentioned accuracy. The cant under consideration is so small that the variation of B_{eff} over the size of the beam is negligible and does not need to be taken into account. The only important tolerance is to provide alignment of the undulator segments in the horizontal direction with an accuracy that allows satisfying the condition $\Delta B_{eff}/B_{eff} \leq 1.5 \times 10^{-4}$. The first proposal discussed, that of a 10 mrad cant, requires a very tight horizontal alignment tolerance (~ 0.1 mm). Alignment in the horizontal direction is more difficult than that in the vertical direction, so different options are examined below and summarized in Table 11.

Table 11. List of possible options for canted pole gap design. ^a

Cant (mrad)	Horizontal alignment accuracy (mm) requirement	$\Delta B_{eff}/B_{eff}$ over 10 mm	Range of horizontal motion (mm) for $\Delta B_{eff}/B_{eff} = \pm 1.5 \times 10^{-3}$ and $\pm 5.5 \times 10^{-4}$ in parenthesis ^b	Thickness steps (mm) of mechanical shims required
2	0.50	3.0×10^{-3}	± 5.0 (± 1.8)	0.010
3	0.33	4.5×10^{-3}	± 3.3 (± 1.2)	0.015
4	0.25	6.0×10^{-3}	± 2.5 (± 0.9)	0.020

^a All calculations were made according to a tolerance of 1.5×10^{-4} and a total range of $\pm 1.5 \times 10^{-3}$ (± 20 Gauss) for $\Delta B_{eff}/B_{eff}$. Spacer thickness steps were chosen to allow full compensation at half the total range of motion.

^b The range of horizontal motion listed in the parentheses corresponds to $\pm 1^\circ\text{C}$ temperature compensation. To allow for temperature compensation of $\pm 1^\circ\text{C}$ the *additional* range of motion listed in parentheses should be provided. The measured temperature dependence of the magnetic field for the prototype undulator was described in section 4.3.3.

All of the options listed in the table look achievable, and we have selected to do testing with a 3 mrad cant. This test will be done in two steps for the current prototype undulator. In the first test, the cant will be implemented by installing mechanical shims between the aluminum base plates and the titanium housing. In the second test, new machined aluminum base plates will be fabricated with the appropriate cant angle. The whole magnetic structure will be re-assembled and tested.

6.3.4 Mechanical Shims

Because one can grind and lap steel shims to a very high incremental accuracy, low-carbon steel shims can be included in the design for the production undulator. (These shims are placed between the aluminum base plate and the housing.) The actual gap setting will be determined by the thickness of the selected shims that can be made with a tolerance of $\sim \pm 2.5 \mu\text{m}$ (manufacturing technology has been checked). The fine tuning of the effective magnetic field will be done with one of the methods described earlier in this section.

7 Costs

The costs associated with the manufacturing of the prototype undulator are summarized in this section.

The costs of the major long-lead-time items (titanium housing, NdFeB magnets, and vanadium permendur poles) and other parts are listed in Table 12. The total cost for the prototype undulator was about \$250K (excluding APS effort).

Table 12. Prototype undulator costs.

Item	Quantity	Cost	Total
Prototype Housing			
Titanium billet	1		\$25K
Machining	1		\$35K
Prototype Magnets			
NdFeB (grade N39SH) ^a	500	\$59	\$30K
Tooling	1		\$12K
Prototype Poles			
Vanadium permendur	460	\$100	\$46K
Other (aluminum base plates, titanium clamps, cam shaft movers, support pillars, alignment system)			\$102K
Total ^b			\$250K

^a For comparison with $\text{Sm}_2\text{Co}_{17}$ magnets (grade R32HS from Shin-Etsu), the estimated cost for 500 magnets is \$125 per magnet.

^b APS effort not included.

8 Appendix

8.1 Appendix A: Engineering Drawings

The AutoCAD engineering drawings and a 3D model are provided on two separate CD-ROMs.

- Disk 1 labeled “LCLS Prototype Undulator, AutoCAD Files, 01/27/04,” contains the engineering drawings.
- Disk 2 labeled “LCLS Undulator 3D Model, ProE Files, 01/27/04,” contains a ProE 3D model and two video files.

Table 13 lists the content of disk 1 containing the AutoCAD engineering drawings.

Table 13. LCLS prototype undulator AutoCAD drawings on CD 1.

ITEM	LEVEL	DRAWING NUMBER	ELECTRONIC FILE NAME	TITLE LINE 1	TITLE LINE 2	LOCATION
1	1	LCLS	LCLSAS.DWG	Undulator	(Prototype)	CD\LCLS
2	2	LCLS.01	LCLS01AS.DWG	Housing	Assembly	CD\LCLS\01
3	3	LCLS.01.01	LCLS0101.DWG	Housing		CD\LCLS\01
4	3	LCLS.01.02	LCLS0102.DWG	Bracket		CD\LCLS\01
5	3	LCLS.01.03	LCLS0103.DWG	Bracket 1		CD\LCLS\01
6	3	LCLS.01.04	LCLS0104.DWG	Pad		CD\LCLS\01
7	3	LCLS.01.05	LCLS0105.DWG	Pad		CD\LCLS\01
8	2	LCLS.02	LCLS02AS.DWG	Magnet Structure	Assembly	CD\LCLS\02
9	3	LCLS.02.01	LCLS0201.DWG	Pole	Assembly	CD\LCLS\02\01
10	4	LCLS.02.01.01	LCLS020101.DWG	Pole		CD\LCLS\02\01
11	4	LCLS.02.01.02	LCLS020102.DWG	Wing		CD\LCLS\02\01
12	4	LCLS.02.01.03	PHANTOM	f 2.38 x 6.4 mm Lg. Pin		LCLS0201 B/M
13	3	LCLS.02.02	LCLS0202.DWG	Plate		CD\LCLS\02
14	3	LCLS.02.03	LCLS0203.DWG	Bar		CD\LCLS\02
15	3	LCLS.02.03R	LCLS0203R.DWG	Bar (additional machining)		CD\LCLS\02
16	3	LCLS.02.04	LCLS0204.DWG	Stopper		CD\LCLS\02
17	3	LCLS.02.04R	LCLS0204R.DWG	Stopper (additional machining)		CD\LCLS\02
18	3	LCLS.02.05	LCLS0205.DWG	Magnet		CD\LCLS\02
19	3	LCLS.02.06	LCLS0206.DWG	Clamp		CD\LCLS\02
20	3	LCLS.02.06-01	LCLS0206-01.DWG	Clamp		CD\LCLS\02
21	3	LCLS.02.06-01R	LCLS0206-01R.DWG	SIDE CLAMP 1		CD\LCLS\02
22	3	LCLS.02.07	LCLS0207.DWG	Clamp		CD\LCLS\02
23	2	LCLS.03	LCLS03AS.DWG	Magnet Structure	Assembly	CD\LCLS\03
24	3	LCLS.03.02	LCLS0302.DWG	Plate		CD\LCLS\03

ITEM	LEVEL	DRAWING NUMBER	ELECTRONIC FILE NAME	TITLE LINE 1	TITLE LINE 2	LOCATION
25	3	LCLS.03.03	LCLS0303.DWG	Bar		CD\LCLS\03
26	3	LCLS.03.03R	LCLS0303R.DWG	Bar (additional machining)		CD\LCLS\03
27		LCLS.03.04	missing	Stopper		
28	3	LCLS.03.04R	LCLS0304R.DWG	Stopper (additional machining)		CD\LCLS\03
29	2	LCLS.04	LCLS04AS.DWG	Magnet Structure	Assembly	CD\LCLS\04
30	3	LCLS.04.02	LCLS0402.DWG	Plate		CD\LCLS\04
31	3	LCLS.04.03	LCLS0403.DWG	Bar		CD\LCLS\04
32	3	LCLS.04.03R	LCLS0403R.DWG	Bar (additional machining)		CD\LCLS\04
33	3	LCLS.04.04	LCLS0404.DWG	Stopper		CD\LCLS\04
34	3	LCLS.04.04R	LCLS0404R.DWG	Stopper (additional machining)		CD\LCLS\04
35	2	LCLS.05	LCLS05AS.DWG	Magnet Structure	Assembly	CD\LCLS\05
36	3	LCLS.05.02	LCLS0502.DWG	Plate		CD\LCLS\05
37	3	LCLS.05.03	LCLS0503.DWG	Bar		CD\LCLS\05
38	3	LCLS.05.03R	LCLS0503R.DWG	Bar - additional machining		CD\LCLS\05
39	3	LCLS.05.03.01	LCLS050301.DWG	SIDE CLAMP 1		CD\LCLS\05
40	3	LCLS.05.03.02	LCLS050302.DWG	SIDE CLAMP 2		CD\LCLS\05
41	3	LCLS.05.04	LCLS0504.DWG	Stopper		CD\LCLS\05
42	3	LCLS.05.04R	LCLS0504R.DWG	Stopper -additional machining		CD\LCLS\05
43	2	LCLS.06	LCLS06AS.DWG	Support	Assembly	CD\LCLS\06
44	3	LCLS.06.01	LCLS0601.DWG	Flange		CD\LCLS\06
45	3	LCLS.06.02	LCLS0602.DWG	Tube		CD\LCLS\06
46	3	LCLS.06.03	LCLS0603.DWG	Flange		CD\LCLS\06
47	2	LCLS.07	LCLS07AS.DWG	Magnet Structure	Assembly	CD\LCLS\07
48	3	LCLS.07.02	LCLS0702.DWG	Plate		CD\LCLS\07
49	3	LCLS.07.03	LCLS0703.DWG	Bar		CD\LCLS\07
50	3	LCLS.07.03R	LCLS0703R.DWG	Bar (additional machining)		CD\LCLS\07
51	3	LCLS.07.04	LCLS0704.DWG	Stopper		CD\LCLS\07
52	3	LCLS.07.04R	LCLS0704R.DWG	Stopper (additional machining)		CD\LCLS\07
53	2	LCLS.08	LCLS08AS.DWG	Single cam actuator	Assembly	CD\LCLS\08
54	3	LCLS.08.01	LCLS0801.DWG	Housing		CD\LCLS\08
55	3	LCLS.08.02	LCLS0802.DWG	Plate		CD\LCLS\08
56	3	LCLS.08.03	LCLS0803.DWG	Cam shaft		CD\LCLS\08
57	3	LCLS.08.04	LCLS0804.DWG	Ring		CD\LCLS\08
58	3	LCLS.08.05	LCLS0805.DWG	Flange		CD\LCLS\08
59	3	LCLS.08.06	LCLS0806.DWG	Cover		CD\LCLS\08
60	3	LCLS.08.07	LCLS0807.DWG	Stopper		CD\LCLS\08
61	3	LCLS.08.08	LCLS0808.DWG	Ring		CD\LCLS\08
62	2	LCLS.09	LCLS09AS.DWG	Double cams actuator	Assembly	CD\LCLS\09
63	3	LCLS.09.01	LCLS0901.DWG	Housing		CD\LCLS\09
64	3	LCLS.09.02	LCLS0902.DWG	Plate		CD\LCLS\09
65	2	LCLS.10	LCLS10AS.DWG	Support	Assembly	CD\LCLS\10
66	3	LCLS.10.02	PHANTOM	14"x14" x .5" Steel Tubing	1012 mm Lg.	LCLS10AS B/M
67	2	LCLS.11	LCLS11AS.DWG	Quadrupole Lens Unit	Assembly	CD\LCLS\11
68	3	LCLS.11.01	LCLS1101.DWG	Quadrupole Lens	Assembly	CD\LCLS\11\01
69	4	LCLS.11.01.01	LCLS110101.DWG	Housing	Assembly	CD\LCLS\11\01\01

ITEM	LEVEL	DRAWING NUMBER	ELECTRONIC FILE NAME	TITLE LINE 1	TITLE LINE 2	LOCATION
70	5	LCLS.11.01.01.01	LCLS110101.DWG	Housing		CD\LCLS\11\01\01
71	5	LCLS.11.01.01.02	LCLS110102.DWG	Insert		CD\LCLS\11\01\01
72	4	LCLS11.01.02	LCLS110102.DWG	Plate		CD\LCLS\11\01
73	4	LCLS.11.01.03	LCLS110103.DWG	Plate		CD\LCLS\11\01
74	4	LCLS.11.01.04	LCLS110104.DWG	Plate		CD\LCLS\11\01
75	4	LCLS.11.01.05	LCLS110105.DWG	Pole		CD\LCLS\11\01
76	4	LCLS.11.01.06	LCLS110106.DWG	Spacer		CD\LCLS\11\01
77	4	LCLS.11.01.07	LCLS110107.DWG	Magnet		CD\LCLS\11\01
78	3	LCLS.11.02	LCLS1102.DWG	Bracket		CD\LCLS\11
79	3	LCLS.11.03	LCLS1103.DWG	Plate		CD\LCLS\11
80	2	LCLS.12	LCLS12.DWG	Screen		CD\LCLS
81	2	LCLS.13	LCLS13.DWG	Flange		CD\LCLS
82	2	LCLS.14	LCLS14.DWG	Stud		CD\LCLS
83	2	LCLS.15	LCLS15.DWG	Bracket		CD\LCLS
84	2	LCLS.15R	LCLS15R.DWG	Bracket-additional machining		CD\LCLS
85	2	LCLS.16	LCLS16.DWG	Bracket		CD\LCLS
86	2	LCLS.16R	LCLS16R.DWG	Bracket-additional machining		CD\LCLS
87	2	LCLS.17	LCLS17.DWG	Screw		CD\LCLS
88	2	LCLS.18	LCLS18.DWG	Stopper		CD\LCLS
89	2	LCLS.29	LCLS29.DWG	Washer		CD\LCLS
90	2	LCLS.33	LCLS33.DWG	Shim Set		CD\LCLS
91	2	LCLS.33A	LCLS33A.DWG	Shim		CD\LCLS
92	2	LCLS.34	LCLS34.DWG	Shim Set		CD\LCLS
93	1	LCLS.50	LCLS50AS.DWG	Assembly Fixture for LCLS	Undulator	CD\LCLS\50
94	2	LCLS.50.01	LCLS5001.DWG	Plate		CD\LCLS\50
95	2	LCLS.50.02	LCLS5002.DWG	Bar		CD\LCLS\50
96	2	LCLS.50.03	LCLS5003.DWG	Bar		CD\LCLS\50
97	2	LCLS.50.04	LCLS5004.DWG	Stopper		CD\LCLS\50
98	2	LCLS.50.05	LCLS5005.DWG	Nut Plate		CD\LCLS\50
99	2	LCLS.50.06	LCLS5006.DWG	Bar		CD\LCLS\50
100	2	LCLS.50.07	LCLS5007.DWG	Bottom Plate		CD\LCLS\50
101	2	LCLS.50.08	LCLS5008.DWG	Spacer Set		CD\LCLS\50

9 References

- ¹ Conceptual Design Report (CDR) for the Linac Coherent Light Source (LCLS) Project, SLAC-R-593, April 2002.
- ² R.J. Dejus, Oleg A. Shevchenko, Nikolai A. Vinokurov, "A Linear Integral-Equation-Based Computer Code for Self-Amplified Spontaneous Emission Calculations of Free-Electron Laser," Nucl. Instrum. Methods A 445 (2000) 19-23.
- ³ E. Gluskin, N.A. Vinokurov, G. Decker, R.J. Dejus, P. Emma, P. Ilinski, E.R. Moog, H.-D. Nuhn, I.B. Vasserman, "Optimization of the design for the LCLS undulator line," Nucl. Instrum. Methods A 475 (2001) 323-327.
- ⁴ E.R. Moog, R.J. Dejus, P.K. Den Hartog, E. Gluskin, E. Trakhtenberg, I. Vasserman, "Design and Manufacture of a Prototype Undulator for the LCLS Project," in Proceedings of the 2001 Particle Accelerator Conference, Chicago, IL, June 18-22, 256-258.
- ⁵ J. Chavanne, P. Elleaume, and P. Van Vaerenbergh, ESRF Machine Tech. Note 1-1996/ID (Jan. 1996).
- ⁶ Argonne National Laboratory Report No. ANL/APS/TB-47, "XFD Progress Report," Section 2.1, December 2002.
- ⁷ M. Petra, P.K. Den Hartog, E.R. Moog, S. Sasaki, N. Sereno, I.B. Vasserman, "Radiation effects studies at the Advanced Photon Source," Nucl. Instrum. Methods A 507 (2003) 422-425.
- ⁸ R.D. Brown and J.R. Cost, J. Appl. Phys. 63 (1988) 3537 and IEEE Trans. Magn. 25 (1989) 3117.
- ⁹ E. Trakhtenberg, V. Tcheskidov, M. Erdmann, I. Vasserman, N. Vinokurov, O. Makarov, and P. Den Hartog, "First Prototype Undulator for the LCLS Project-Mechanical Design and Prototype Lessons," 2nd International Workshop on Mechanical Engineering Design of Synchrotron Radiation Equipment and Instrumentation (MEDS102) Argonne National Laboratory, Argonne, IL, September 5-6, 2002.
- ¹⁰ B. Brajuskovic, P. Den Hartog, E. Trakhtenberg, "Mechanical analysis of the prototype undulator for the Linac Coherent Light Source," in Proceedings of the 2003 Particle Accelerator Conference, Portland, OR, May 12-16, 1017-1019.
- ¹¹ "Guide to Machining Carpenter Stainless Steels and Specialty Metals," Carpenter Technology Corporation, 1993, USA.
- ¹² O.A. Makarov, V.G. Tcheskidov, E.M. Trakhtenberg, "Positioning System for the LCLS Undulator," Nucl. Instrum. Methods A 507 (2003) II-25.
- ¹³ I. Vasserman, S. Sasaki, R. Dejus, E. Moog, E. Trakhtenberg, N. Vinokurov, "Measurement, sorting, and tuning of LCLS undulator magnets," Nucl. Instrum. Methods A 483 (2002) 383-387.
- ¹⁴ I.B. Vasserman, S. Sasaki, R.J. Dejus, O.A. Makarov, E.R. Moog, E.M. Trakhtenberg, N.A. Vinokurov, "Magnetic measurements and tuning of the LCLS prototype undulator," Nucl. Instrum. Methods A 507 (2003) 191-195.
- ¹⁵ I. Vasserman, Argonne National Laboratory Report No. ANL/APS/TB-32, "Test of Horizontal Field Measurements Using Two-Axis Hall Probes at the APS Magnetic Measurement Facility," January 1998.
- ¹⁶ O. Chubar, P. Elleaume, J. Chavanne, "A 3D Magnetostatics Computer Code for Insertion Devices," J. Synch. Rad. 5 (1998) 481.

-
- ¹⁷ Web URL: http://www.esrf.fr/machine/groups/insertion_devices/Codes/Radia/Radia.html
- ¹⁸ A. Zeller, "Radiation Damage in Permanent Magnetic Materials," National Superconducting Cyclotron Laboratory Report (1999).
- ¹⁹ J. Cost, R. Brown, A. Giorgi and J. Stanley, "Radiation Effects in Rare Earth Permanent Magnets," Proc. Materials Research Society Symposium, Vol. 96, (1987) 321-327.
- ²⁰ A. Zeller and J. Nolen, "Radiation and Temperature Effects on Sm-Co and NdFeB Magnets in Low Permeance Configurations," 9th International Workshop on Rare Earth Magnets and their Applications, FRG (1987) 157-162.
- ²¹ S. Okuda, K. Ohashi and N. Kobayashi, "Effects of Electron Beam and γ -ray Irradiation on the Magnetic Flux of NdFeB and SmCo Permanent Magnets," Nucl. Instrum. Methods B 94 (1994) 227-230.
- ²² P. Colomp, T. Oddolaye and P. Elleaume, "Demagnetization of Permanent Magnets to 180 MeV Electron Beam," ESRF/MACH-ID/93-09.
- ²³ H. Luna et al., "Bremsstrahlung Radiation Effects in Rare Earth Permanent Magnets," Nucl. Instrum. Methods A 285 (1989), 349-354.
- ²⁴ T. Bizen et al., "Demagnetization of Undulator Magnets Irradiated with High Energy Electrons," Nucl. Instrum. Methods A 467-468 (2001) 185-189.
- ²⁵ T. Bizen et al., "Introduction of the High Radiation Resistance of Undulator Magnet," presented at the 8th International Conference on Synchrotron Radiation Instrumentation, CA, 2003, to be published.
- ²⁶ T. Bizen et al., "Improvement of Radiation Resistance of NdFeB Magnets by Thermal Treatment," presented at the 8th International Conference on Synchrotron Radiation Instrumentation, CA, 2003, to be published.
- ²⁷ Shin-Etsu, vendor specifications. Private communication.
- ²⁸ I. Vasserman, R. Dejus, N. Vinokurov, "Phasing of the Insertion Devices at the APS FEL Project," AIP Conf. Proc., 521 (AIP, 2000) 368-371.